

1

2

3 **Hydrothermal activity along the slow-spreading Lucky Strike ridge segment**  
4 **(Mid-Atlantic Ridge): Distribution, heatflux, and geological controls**

5

6

7 J. Escartin<sup>1\*</sup>, T. Barreyre<sup>2</sup>, M. Cannat<sup>1</sup>, R. Garcia<sup>3</sup>, N. Gracias<sup>3</sup>, A. Deschamps<sup>4\*</sup>, A. Salocchi<sup>5</sup>,  
8 P.-M. Sarradin<sup>6</sup>, and V. Ballu<sup>7</sup>

9

10

11

12 <sup>1</sup>Laboratoire de Géosciences Marines, IPGP, CNRS UMR7154, Paris, France

13 <sup>2</sup>Woods Hole Oceanographic Institution, Woods Hole, MA, USA

14 <sup>3</sup>VICOROB, University of Girona, Spain

15 <sup>4</sup>Laboratoire Domaines Océaniques, CNRS & Université de Bretagne Occidentale, Brest, France

16 <sup>5</sup>University of Modena and Reggio Emilia, Modena, Italy

17 <sup>6</sup>EEP, IFREMER, Brest, France

18 <sup>7</sup>Université de La Rochelle, La Rochelle, France

19

20 \*Corresponding author: Javier Escartin – [escartin.javier@gmail.com](mailto:escartin.javier@gmail.com)

21

22

23

24

25 \*Note: This article is dedicated to the memory and contributions of the co-author Anne  
26 Deschamps, who passed-away in late 2014 during the preparation and writing of this  
27 manuscript.

## 28 **Abstract**

29 We have reviewed available visual information from the seafloor, and recently acquired  
30 microbathymetry for several traverses across the Lucky Strike segment, to evaluate the  
31 distribution of hydrothermal activity. We have identified a new on-axis site with diffuse  
32 flow, Ewan, and an active vent structure ~1.2 km from the axis, Capelinhos. These sites  
33 are minor relative to the Main field, and our total heatflux estimate for all active sites  
34 (200-1200 MW) is only slightly higher than previously published estimates. We also  
35 identify fossil sites W of the main Lucky Strike field. A circular feature ~200 m in  
36 diameter located on the flanks of a rifted off-axis central volcano, is likely a large and  
37 inactive hydrothermal edifice, named Grunnus. We find no indicator of focused  
38 hydrothermal activity elsewhere along the segment, suggesting that the enhanced melt  
39 supply and the associated melt lenses, required to form central volcanoes, also sustain  
40 hydrothermal circulation to form and maintain large and long-lived hydrothermal fields.  
41 Hydrothermal discharge to the seafloor occurs along fault traces, suggesting focusing of  
42 hydrothermal circulation in the shallow crust along permeable fault zones.

43

## 44 **1. Introduction and geological setting**

45 Hydrothermal activity along mid-ocean ridges controls cooling of the oceanic  
46 lithosphere, and impacts its thermal structure and the processes operating there (e.g.,  
47 magmatic emplacement, faulting, seismicity, diking and melt delivery to the seafloor).  
48 Understanding the distribution of hydrothermal activity and its nature is necessary to  
49 quantify the associated heatflux, its partition between diffuse and focus flow  
50 recognizable at the seafloor, and to evaluate the amount of cooling withno expression at  
51 the seafloor (e.g., conductive cooling or low-temperature, diffuse percolation).

52 Slow spreading ridge sections with significant melt supply typically define linear ridge  
53 segments with lengths of a few tens of km to up to ~100 km. These segments typically  
54 develop ridge-parallel normal faults on both flanks, and thick crust at their center  
55 indicating melt-focusing along-axis. As in the case of the Lucky Strike segment, sustained  
56 volcanism may lead to the development of central volcanoes (Escartín et al., 2014). The  
57 slow-spreading Lucky Strike segment is unique in that it has been extensively studied  
58 during more than two decades, following the discovery of the Lucky Strike hydrothermal  
59 field, from hereon referred to as the Main Lucky Strike hydrothermal field (MLSHF),  
60 located at its segment center and at the summit of the central volcano (Langmuir et al.,

61 1997). This is one of the most extensive hydrothermal fields discovered to date, and it is  
62 located along a recent graben dissecting the Lucky Strike central volcano(Humphris et  
63 al., 2002; Ondréas et al., 2009; Barreyre et al., 2012; Escartín et al., 2014). Water-column  
64 studies have also revealed hydrothermal plumes at greater depths than that of the  
65 MLSHF (Wilson et al., 1996; German et al., 1996; Thurnherr et al., 2008). These authors  
66 proposed a yet unidentified source at the southern end of the segment and at a depth of  
67 2000 m.

68 A ~3-3.5 km deep magma chamber(Singh et al., 2006)at the base of a ~600 m thick  
69 Layer 2A (Seher et al., 2010) underlies The MLSHF (Figure 2). Major faults within the rift  
70 valley(Escartín et al., 2014) can be linked to fault reflectors that do not reach the magma  
71 chamber depth in seismic reflection profiles(Combi et al., 2015).Microseismicity  
72 below the hydrothermal field(Crawford et al., 2013)is unrelated to these fault reflectors,  
73 and likely corresponds to hydrothermal cooling instead (Figure 3).

74 In this paper we provide a synthesis of available information along the Lucky Strike  
75 ridge segment, from seafloor observations and imagery to microbathymetricand  
76 acoustic data (Figure 1).We analyze these data to identify and map new hydrothermal  
77 sites, and use other observables (presence of a magma chamber, microseismicity,  
78 faulting) to constrain the processes controlling distribution and location of hydrothermal  
79 activity along this segment, to evaluate heat fluxes at the segment scale, and to discuss  
80 the implications for heat extraction and magmatic supply. Finally, we review evidence of  
81 hydrothermal activity along the segment based on water-column studies.

82

## 83 **2. Data and indicators of hydrothermal activity at the seafloor**

84 The Lucky Strike area has been targeted by numerous cruises in the last 25 years,  
85 providing extensive visual information from direct human observations, video imagery,  
86 and electronic still-camera images acquired with human-operated vehicles (HOVs),  
87 remotely operate vehicles (ROVs), and deep-towed camera systems. These visual  
88 observationsare complemented with near-bottom high-resolution bathymetry data  
89 acquired both with ROVs and Autonomous Underwater Vehicles (AUVs) during cruises  
90 in 2008 and 2009, in addition to a prior deep-towed sonar survey (Scheirer et al., 2000;  
91 Humphris et al., 2002; Escartín et al., 2014), as summarized inFigure 1 and  
92 Supplementary Table 1.Near-bottom ROV and AUV bathymetry data have a resolution of  
93 several decimeters to a few meters per pixel, depending on survey altitude, and provide

94 detailed information on theseafloor texture that can be used to discriminate between  
95 hydrothermal structures (e.g., hydrothermal mounds and chimneys, Figure 2) from  
96 other structures whose origin is instead volcanic (e.g., hummocks, lava channels and  
97 flows), tectonic (e.g., faults, fissures), or related to secondary mass-wasting processes  
98 (e.g., landslides along fault scarps).

### 99 *2.1. Visual observations*

100 The bulk of the field work involving visual observations at the seafloor focuses on the  
101 MLSHF, which is yearly visited since 2008 (MoMAR08) and is instrumented for  
102 monitoring since 2010 as part of the MOMARSAT European Multidisciplinary Seafloor and  
103 water column Observatory (EMSO) deep-sea seafloor observatory (Colaço et al., 2011).  
104 In this study we use imagery and visual observations along with HOV, ROV, and deep-  
105 towed camera systems (Figure 1a) that extend both along the Lucky Strike segment, and  
106 across the full rift valley width (Figure 1a), and present a large-area seafloor  
107 photomosaics from vertically-acquired imagery. The first systematic survey of the  
108 MLSHF was conducted with ARGO II towed-camera in 1996 (Humphris et al., 2002;  
109 Escartin et al., 2008). Subsequent surveys conducted with the ROV VICTOR low-light  
110 camera covered fully the MLSHF (Barreyre et al., 2012), extending beyond prior surveys,  
111 and South along the ridge axis (Figure 1). Vertical imagery was processed into a single  
112 georeferenced seamless giga-mosaic. Details on the ARGO II and OTUS image surveys at  
113 MLSHF, and on image processing and mosaicing are provided elsewhere (Escartín et al.,  
114 2008; Barreyre et al., 2012; Prados et al., 2012); here we present for the first time the  
115 2009 photomosaic ~1 km south of the MLSHF.

116 Active hydrothermal sites are readily identifiable visually from venting fluids (high-  
117 temperature black smokers and clear-fluid vents, diffuse outflow at lower  
118 temperatures), hydrothermal macrofauna and microbial communities (e.g., bacterial  
119 mats and mussel beds), or white anhydrite deposits that require venting temperatures of  
120 120-150°C (Bischoff and Seyfried, 1978). These visual features have been used to  
121 extensively map the MLSHF from both photomosaics and oblique-view imagery acquired  
122 with ROVs or HOVs (Barreyre et al., 2012). Fossil hydrothermal outflow areas are also  
123 recognizable by fossil chimneys, sulfide rubble, and hydrothermal staining, which are  
124 clearly distinguishable from basalt or sediment (Lalou et al., 1989; Barreyre et al., 2012).

125 Supplementary Table 1 and Figure 1 provide an overview of the seafloor visually  
126 explored along >900 km of submersible tracks at the Lucky Strike segment, largely  
127 concentrated at the segment center and the MLSHF. The seafloor photomosaics

128 (Barreyre et al., 2012) image  $\sim 1.5$  km<sup>2</sup> of seafloor centered on the MLSHF, and  $\sim 0.4$   
129 km<sup>2</sup> on-axis  $\sim 2$  km south of MLSHF. Seafloor observations outside the MLSHF were  
130 conducted primarily during the 1994 DIVA cruise (Fouquet et al., 1994; Ondreas et al.,  
131 1997) with both HOV Nautille and Scampi camera tows to the North, during the 2006  
132 Graviduck cruise (HOV and camera tows), and during ROV dives in subsequent cruises  
133 (Supplementary Table 1). In this paper the visual indicators of hydrothermal activity are  
134 from shipboard observations (cruise reports and published results), and from a  
135 systematic review of ROV and HOV video imagery and seafloor photography available to  
136 us (cruises underlined in Supplementary Table 1).

137

### 138 *2.2. Microbathymetric data*

139 Microbathymetric data acquired in 2006 (MOMARETO cruise, Supplementary Table  
140 1) (Ondreas et al., 2009), was complemented with MOMAR'08 and Bathyluck'09 surveys  
141 using ROV VICTOR6000 equipped with a RESON 7150 multibeam system, and AUV  
142 Aster-X equipped with a SIMRAD EM2000 multibeam system. After data processing  
143 (ping editing, correction of navigation, filtering, and gridding), the final  
144 microbathymetric grids have a pixel resolution that varies between 25 cm and 2 m per  
145 pixel depending on survey altitude.

146 The MOMAR'08 and Bathyluck'09 surveys were conducted at the segment center and  
147 over the central volcano summit, across the rift valley floor at different locations along  
148 the segment, and at the flank of the southwestern inside corner of the segment end  
149 (Figure 1). The combined set of microbathymetric surveys, which cover  $\sim 35$  km<sup>2</sup> of the  
150 Lucky Strike segment seafloor, is one of the most extensive microbathymetry surveys  
151 along a slow-spreading ridge segment, and complements a prior  $\sim 190$  km<sup>2</sup> high-  
152 resolution sonar survey (Scheirer et al., 2000a; Escartín et al., 2014). For this study we  
153 analyzed shaded relief and slope maps of the microbathymetric dataset to identify the  
154 seafloor morphology consistent with that of hydrothermal deposits, as described below.

155

### 156 *2.3. Acoustic backscatter data*

157 The central portion of the Lucky Strike segment was surveyed with the DSL120 deep-  
158 towed, near-bottom high-resolution sonar system (Scheirer et al., 2000; Humphris et al.,  
159 2002). These data have been re-processed and presented elsewhere (Escartín et al.,  
160 2014), together with an interpretation of the tectonic and volcanic structure of this

161 portion of the Lucky Strike segment. Sonar data are shifted locally to match the  
162 microbathymetry, as the navigation of the DSL120 towed vehicle is less accurate than  
163 that of ROV or AUVs used in microbathymetric surveys. By themselves sonar data are  
164 not sufficient to identify hydrothermal deposits. First, sulfides do not display acoustic  
165 properties that are distinct from basaltic basemen.. Second, acoustic backscatter  
166 depends on numerous parameters such as insonification direction and angle, acoustic  
167 shading, sedimentation, and instrumental artifacts, among other factors. In this study we  
168 only use acoustic backscatter to support the interpretation of the microbathymetric data.

169

#### 170 *2.4. Identification and extent of hydrothermal sites and fields*

171 Hydrothermal activity with high-temperature fluid discharge ubiquitously displays  
172 mounds and chimneys that can reach up to a few tens of meters above surrounding  
173 seafloor, with basal widths of meters to a few tens of meters (Figure 2). Areas with  
174 hydrothermal vents have a characteristic microbathymetric signature, with spikes and  
175 small-scale lumps, that corresponds to the “lumpy” seafloor morphology described  
176 previously for the MLSHF(Ondreas et al., 2009) (Figure 2a), and for other hydrothermal  
177 fields along mid-ocean ridges (Ferrini et al., 2008; Jamieson et al., 2014) elsewhere  
178 (Figure 2b). This lumpy terrain can be clearly differentiated from the volcanic seafloor  
179 morphology (hummocks, lava flows, lava channels) that tends to be spatially larger  
180 structures (tens to hundreds of m) and that displays instead a smooth seafloor  
181 morphology lacking spikes.

182 Zones with rubble, which are systematically found along slopes of fault scarps or  
183 volcanic structures, show instead a granulated texture due to individual rock blocks,  
184 which are systematically smaller than hydrothermal structures (~1-2 m or less, Figure  
185 2a). This hydrothermal seafloor texture, which is common to hydrothermal fields (e.g.,  
186 Lau Basin, Figure 2b)(Ferrini et al., 2008; Jamieson et al., 2014), is used here to map the  
187 extent of hydrothermal sites within a hydrothermal field, or of new hydrothermal  
188 fields.High-resolution acoustic backscatter, which can reveal this ‘lumpy’ hydrothermal  
189 terrain under optimal insonification conditions, is used to complement the  
190 microbathymetry.

191 Imagery(Figure 1a) is critical to confirm that sites identified in the microbathymetry do  
192 correspond to hydrothermal deposits, active or inactive. It is also required to map areas  
193 of diffuse hydrothermal outflow, young hydrothermal activity, or fossil structures, with

194 no clear morphological signature (bacterial mats, vents, hydrothermal staining, dead  
195 chimneys, etc.). Extensive seafloor photomosaics are available for the MLSHF, where the  
196 hydrothermal activity has been extensively mapped (Barreyre et al., 2012), and  
197 additional photomosaics are available for an area ~2 km south of this site, along the  
198 ridge axis (Figure 1a). The rest of the imagery is acquired along HOV, ROV, or tow tracks  
199 (Figure 1a), which is adequate to identify areas of hydrothermal activity but cannot be  
200 used to properly constrain the extent and limits of these areas.

201 Hence, the areas of 'lumpy' hydrothermal terrain identified in this study, based on  
202 microbathymetric data (Figure 1b), indicate zones of significant and sustained  
203 hydrothermal activity with significant sulfide accumulation. The bathymetric data also  
204 reveal numerous volcanic features (hummocks, volcanic cones), tectonic structures  
205 (fault scarps and fissures), and mass wasting indicators (slump scars, debris flows, scree,  
206 dejection cones).

207 Water column studies have also been used to identify hydrothermal activity. High-  
208 temperature black smoker type fluids form buoyant plumes in the water column that  
209 can be detected from turbidity and manganese anomalies (Klinkhammer et al., 1985;  
210 Baker et al., 2001; Baker, 2007; German et al., 2010), while methane anomalies can be  
211 associated with sites showing both high-temperature venting (Lupton, 1990) and low-  
212 temperature serpentinization (Bougault et al., 1993; Charlou and Donval, 1993; Gràcia et  
213 al., 2000). The observations and datasets (microbathymetry, imagery, water column  
214 studies) available along the Lucky Strike segment show thus limitations in the ability to  
215 detect diffuse and very low-temperature outflow or conductive cooling, that are not  
216 associated with either sulfide mounds (Figure 2) or with visual indicators of  
217 hydrothermal activity (bacterial mats, anhydrite and other hydrothermal mineral  
218 deposits).

219

### 220 **3. Hydrothermal sites at the Lucky Strike segment**

221 Based on both the imagery and the microbathymetry shown in Figure 1, we have  
222 characterized the distribution and nature of hydrothermal discharge throughout the rift  
223 valley floor of the Lucky Strike segment. The distribution of hydrothermal activity and  
224 deposits of the Main Lucky Strike hydrothermal field have been mapped in recent  
225 studies (Ondréas et al., 2009; Barreyre et al., 2012). Using the new microbathymetric  
226 data we have identified additional hydrothermal deposits at the western edge of

227 this main hydrothermal field and extended its limits (Figure 3, Table 1). We also report  
228 three additional hydrothermal sites along the Lucky Strike segment (Figure 3). Two out  
229 of these three new sites, Ewan and Capelinhos, have been visited and are confirmed to be  
230 active. The third site at the MLSHF has been visited and confirmed to be inactive (H6;  
231 Figure 4). The fourth site, Grannus, has been identified solely from the microbathymetric  
232 seafloor texture, but lacks direct visual observations to determine if it is active or  
233 inactive, or what may be the nature of the associated hydrothermal deposits.

234

### 235 *3.1. Main Lucky Strike hydrothermal field (MLSHF)*

236 The MLSHF has been systematically mapped and studied during the last two decades  
237 since its discovery in the 90's (Supplementary Table 1) (Langmuir et al., 1997; Humphris  
238 et al., 2002; Escartín et al., 2008; Ondréas et al., 2009; Barreyre et al., 2012; Barreyre et  
239 al., 2014b; Mittelstaedt et al., 2012). Microbathymetry acquired during the Momareto'06  
240 survey has been used to identify the extent, nature, and limits of several areas  
241 corresponding to hydrothermal deposits and associated debris (1 through 4 in Figure 3,  
242 Table 1). This morphological mapping is complemented by large-area seafloor  
243 photomosaics (Escartín et al., 2008; Barreyre et al., 2012; Mittelstaedt et al., 2012;  
244 Prados et al., 2012), used to determine the distribution of both fossil and active venting  
245 (Barreyre et al., 2012) both within these hydrothermal areas and elsewhere throughout  
246 the field (Figure 3).

247 The data collected during the MOMAR'08 and Bathyluck'09 cruises reveal two new  
248 hydrothermal areas at the MLSHF (Areas 5 and 6 in Figure 3). Area 5, which is located in  
249 the southwestern part of the MLSHF and within the axial graben (Figure 3, Table 1), is  
250 associated with zones of diffuse flow and scattered active and inactive vents that are  
251 visible in the microbathymetry.

252 Area 6 is located ~1.5 km from the center axis at the western edge of the MLSHF, and in  
253 the immediate vicinity of the main fault scarp bounding the axial graben. The seafloor in  
254 this area, which corresponds to the flank of an axial volcano recently rifted, is cross-cut  
255 by small-scale normal faults with vertical displacements of up to a few meters, and with  
256 'lumpy' hydrothermal seafloor texture (Figures 3, 4). Area 6a corresponds to a broad  
257 mound with several spikes (vents) extending over an area of ~70x70 m (Figure 4), and  
258 that buries a normal fault scarp that is visible towards the North. Areas 6b and 6c, which  
259 had been previously identified in microbathymetric data (Ondréas et al., 2009), are



260 smaller and show instead several isolated spikes and no clear mound. Observations from  
261 VICTOR#605 dive (MOMARSAT'15 cruise, Figure 4) found no evidence of active  
262 hydrothermal activity, but confirmed that the pinnacles correspond to fossil  
263 hydrothermal chimneys (Figure 4c), and that the area displays numerous indicators of  
264 fossil hydrothermal outflow such as smaller hydrothermal mounds (Figure 4d),  
265 hydrothermal staining, sulfide rubble, shell chaff, and hydrothermal slab similar to that  
266 found at the center of the MLSHF.

### 267 3.2. Ewan

268 The Ewan hydrothermal field was serendipitously discovered during HOV Nautilie dive  
269 1624 (Graviluck 2006 cruise, Supplementary Table 1). This dive crossed a series of  
270 seafloor patches covered with filamentous bacterial mats that are white and highly  
271 reflective when illuminated, associated with mussel beds, and primarily found along  
272 scarps and slopes covered with rubble and sediment (Figure 5a-c). Following its  
273 discovery, the site was fully surveyed to obtain seafloor photomosaics and  
274 microbathymetry (Figures 5d-g, MOMAR'08 and Bathyluck'09 cruises, Supplementary  
275 Table 1). Ewan is located within the axial graben dissecting the central volcanic  
276 cone (Escartín et al., 2014), ~2 km south of the MLSHF (Figures 3 and 5f). The seafloor  
277 here displays a complex set of horst and graben (Figure 5f), with numerous east- and  
278 west-verging normal faults that confine the most recent, unsedimented lava  
279 flows (Escartín et al., 2014).

280 In the photomosaics bacterial mats correspond to white areas with a mottled seafloor  
281 aspect (Figures 5c-d), with irregular and gradational limits. Owing to the resolution of  
282 the photomosaics (5-10 mm per pixel), we can also identify macrofauna associated with  
283 the vents (e.g., fish, Figure 5e), but mussel beds associated with the bacterial mats are  
284 not visible in this imagery. Using mapping techniques and interpretation developed  
285 earlier (Barreyre et al., 2012), we identified and digitized ~150 larger patches, in  
286 addition to >400 that are too small to be digitized, and for which we only record their  
287 position. The ~150 digitized patches cover ~275 m<sup>2</sup>, while the rest correspond to ~30  
288 m<sup>2</sup>, attributing 0.06 m<sup>2</sup> to each of the smaller features (~0.25x0.25 m<sup>2</sup>). These estimates  
289 (Table 2) are likely minima as topography is not accounted for (flat projection), and the  
290 photomosaic have gaps where active areas may occur.

291 Ewan contains several clusters of bacterial mats along a NNE-SSW direction, extending  
292 ~250 m along-axis and ~40 m across axis, and in the continuation of aligned pits ~10 m  
293 deep and ~30 m wide (Figure 4g). Bacterial mats occur both along slopes (pits, fault

294 scarps, Figure 5a-c) and flat-lying, volcanic seafloor (ropy lavas, RL, in Figure 5d).  
295 Detailed HOV observations (Figure 3c) revealed shimmering locally, as observed in  
296 diffuse outflow areas at the MLSHF. We did not find active nor fossil high-temperature  
297 venting (e.g., active or fallen chimneys) during the HOV dive or in the seafloor  
298 photomosaics, suggesting that Ewan hosts only diffuse hydrothermal activity. The  
299 distribution and shape of individual bacterial patches also indicates fluid percolation  
300 through the seafloor at very slow flow rates.

301

### 302 *3.3. Capelinhos*

303 Capelinhos is a vent field located ~1.5 km E of the MLSHF, on the western, outward-  
304 dipping flank of a summital volcanic cone (Figures 3 and 6) first identified in the  
305 microbathymetric data (Bathyluck'09 cruise). The site was first visited during an ROV  
306 dive in 2013 (MoMARSAT'13 cruise, Supplementary Table 1), which confirmed its  
307 activity. The microbathymetry shows a main hydrothermal mound that peaks ~20 m  
308 above the surrounding seafloor, centered along the trace of a small fault scarp and  
309 fissure now buried by the hydrothermal deposits (Figure 6d). This hydrothermal edifice,  
310 which links with nearby structures that rise a few meters to 10 m above surrounding  
311 seafloor (Figure 6d), shows a low acoustic backscatter and lacks any clear texture in the  
312 sonar imagery (Figure 6e). ROV dives (Figure 6d) have confirmed the presence of both  
313 inactive and active chimneys with high-temperature outflow through black smokers,  
314 clear vents, and flanges (Figure 6a-c). Visual observations suggest that diffuse flow is  
315 limited at this site, but we lack seafloor photomosaics to accurately evaluate the type,  
316 geometry, and distribution of diffuse flow as done for Ewan and the MLSHF.

317 At a distance of 150 m to the southwest of the Capelinhos vent the bathymetry shows a  
318 ~50 m diameter dome rising ~2-3 m above surrounding seafloor, which has not been  
319 visited to date (Figure 6d). Nearby fissures immediately to the north expose layered  
320 deposits, reminiscent of hyaloclastite layers blanketing the MLSHF (Ondreas et al., 1997;  
321 Ondreas et al., 2009). This structure is located in the immediate vicinity of the fault  
322 buried by Capelinhos, and its associated acoustic backscatter is low and the sonar  
323 featureless, as observed for the main vent structure (Figure 6e). A hydrothermal origin  
324 is inconsistent with its surface morphology, which lacks the typical 'spikes' found in  
325 hydrothermal terrain. Irregular terrain found East of Capelinhos is instead of volcanic  
326 origin (Figures 6d and e). ROV observations in the area show a sedimented seafloor with  
327 pillows visible locally, with no evidence of standing hydrothermal chimneys or mounds,

328 and possible hydrothermal staining that is local and minor, and that has not been  
329 sampled. The associated sonar imagery shows a hummocky volcanic texture that is  
330 common along the axial seafloor of the Mid-Atlantic Ridge (Smith and Cann, 1990; Yeo et  
331 al., 2011).

332

### 333 *3.4. Grunnus*

334 Microbathymetric data and sonar imagery show a possible off-axis hydrothermal field,  
335 named Grunnus (Figure 7), ~2.5 km west of the MLSHF and corresponding to a  
336 spreading age of ~220 kyrs (Table 1). This structure has a diameter of ~200 m, with  
337 steep flanks, and a platform ~40-50 m above the surrounding seafloor to the S, and that  
338 abuts against the coalescing volcanic cones and hummocks on the flanks of the rifted  
339 central volcano to the north. This platform hosts a 20-m high structure that casts a clear  
340 shadow in the sonar imagery towards the E (Figure 7b). The shape and size of Grunnus  
341 is reminiscent of that of the TAG hydrothermal mound, which has a pancake shape ~200  
342 m in diameter and ~50 m in height (Humphris and Kleinrock, 1996). Microbathymetry  
343 and the sonar data show by small-scale rugosity and pinnacles at its surface that we  
344 attribute to hydrothermal structures (chimneys, mounds). The volcanic mounds to the  
345 north display instead a smooth surface (Figure 7).

346 While the mound at Grunnus has not been visited, we suggest that this off-axis site is  
347 likely inactive. Observations during an HOV dive conducted in 2006 (Graviluck'06 cruise,  
348 Figure 7a) that approached the base of Grunnus yielded no evidence of hydrothermal  
349 deposits, activity, nor indicators of present or past fluid flow. Furthermore, water  
350 column studies nearby (Wilson et al., 1996; Thurnherr et al., 2008) lack a hydrothermal  
351 plume signature, and seismic reflection and refraction data (Singh et al., 2006; Crawford  
352 et al., 2010; Combi et al., 2015) do not image an underlying AMC that may act as a heat  
353 source for an active hydrothermal field.

354 Bathymetry and sonar imagery also show a fault cross-cutting the western flank of the  
355 mound. The fault scarp is well defined and sharp towards the southwest of the mound,  
356 where it shows up to ~5 m of vertical throw and crosscuts seafloor lacking  
357 hydrothermal texture. Across the mound this fault scarp is recognizable but is not as  
358 well-defined, suggesting that deformation postdated mound emplacement and growth.  
359 The difference in fault morphology and height between the mound and surrounding

360 seafloor may be attributed to the different mode of faulting in poorly consolidated  
361 hydrothermal deposits relative to basaltic seafloor.

362

363

#### 364 **4. Discussion**

##### 365 *4.1 Magmatic controls on distribution of hydrothermal activity*

366 The review and analysis of seafloor imagery and microbathymetric data along the Lucky  
367 Strike segment (Figure 1) has allowed us to map new areas with fossil hydrothermal  
368 deposits at the western edge of the MLSHF. The location of the four sites at the segment  
369 center, and the lack of any visual or bathymetric indicators of hydrothermal activity  
370 elsewhere along the segment, suggest a link between melt focusing to the segment center  
371 and heat sources stable over long periods of time generating hydrothermal activity. Our  
372 results do not preclude hydrothermal activity elsewhere, that would be undetected in  
373 the absence of visual imagery (diffuse venting with no morphologic signature), in areas  
374 imaged but lacking detailed observations to detect low-temperature flow that is not  
375 associated with bacterial mats or anhydrite deposits, or in areas where no near-bottom  
376 data exists (see section 4.4. for discussion of water column studies).

377 Of the three active fields, MLSHF and Ewan are at the summit of the central volcano,  
378 along the axial graben dissecting it (Ondréas et al., 2009; Escartín et al., 2014), and  
379 immediately above the ~3-3.5 km deep axial magma chamber (AMC) (Singh et al., 2006;  
380 Combier et al., 2015). The AMC is not centered at the present-day ridge axis, and both  
381 Ewan and MLSHF are located towards its eastern edge, while Capelinhos is located ~700  
382 m east of the AMC's edge (Figure 3 and 8). The AMC also extends ~6 km along-axis,  
383 likely imparting a three-dimensional thermal structure where temperature gradients  
384 can focus flow towards the segment center (Fontaine et al., 2011).

385 The off-axis Grunnus field is on a volcano flank originally emplaced at the Lucky Strike  
386 segment center and since rifted. The original setting is thus similar active on- and near-  
387 axis fields along this segment (MLSHF, Ewan, and Capelinhos, Figure 3). It is likely that,  
388 as in the case of the hydrothermally active segment center, the Grunnus field may have  
389 been animated by a magma chamber underlying the rifted central volcano at the time of  
390 its formation, both now extinct.

391

393 *4.2 Faulting, permeability structure, and outflow at the seafloor*

394 Figure 8 presents a schema of fluid flow within the upper crust associated with the  
395 active hydrothermal fields at the active Lucky Strike hydrothermal field, based on  
396 geological observations and geophysical data. First, the permeability of the crust  
397 immediately above the AMC is likely lower than that of the shallow crust Layer  
398 2A(Barreyre et al., 2014a)owing to its composition and the confining pressure(Figure 8).  
399 This crustal section must host the hydrothermal upwelling animated by the presence of  
400 the AMC, likely to be distributed and in the form of broad hydrothermal plumes of up to  
401 1 km in diameter for reasonable crustal permeabilities (Fontaine et al., 2014), as shown  
402 in Figure 8.

403 Second, fluid flow at the seafloor is not broadly distributed, but localized along or  
404 nearfaults. This has been welldocumented for individual vents and areas of diffuse flow  
405 within the MLSHF through detailed hydrothermal and tectonic mapping (Barreyre et al.,  
406 2012), and for the newly discovered active sites. Ewan is set on tectonic depressions  
407 within the axial graben (Figure 5), while the Capelinhos edifice and associated  
408 structures are set at the continuation of fault traces visible in surrounding seafloor  
409 (Figure 6), covered subsequently by hydrothermal deposits. This association between  
410 hydrothermal outflow and faults, widely observed at other deep-sea hydrothermal fields  
411 at all spreading ridges and in different tectonic environments(Kleinrock et al., 1993;  
412 Haymon et al., 2005; Pedersen et al., 2010; Marcon et al., 2013),suggests that permeable  
413 faultschannel hydrothermal flow in the shallow crust(Barreyre et al., 2012; Barreyre et  
414 al., 2014a), as illustrated in Figure 8.

415 Rifting and diking at the Lucky Strike segment center have concentrated along the ~1  
416 km-wide axial graben dissecting the Lucky Strike central volcano(Humphris et al., 2002;  
417 Ondréas et al., 2009; Escartín et al., 2014). These processes may play an important role  
418 in the permeability of the crust overlying the AMC, with the development of a zone of  
419 high-permeability following the axial graben, and induced by thermal cracking and  
420 fracturing associated with dike emplacement, and by small-scale faulting that is likely  
421 limited to the shallowest 1-2 km of the crust (Figure 8). An anisotropic permeability  
422 structure, coupled with a magma chamber, can promote along-axis convection cells  
423 (Fontaine et al., 2014) consistent with microseismicity clusters observed here above the  
424 AMC (Crawford et al., 2013), with clusters resulting from cracking-induced  
425 microseismicity induced by cooling. It is thus likely that the two microseismicity clusters

426 along the axial graben, one immediately north of the MLSHF, and the second below the  
427 summit of the axial volcanic cone (Figure 3) correspond to cooling in downflow  
428 areas. Venting at Capelinhos, which is East of the AMC edge, is then likely associated to  
429 flow along a permeable fault that may root at the main upwelling zone and below the  
430 Layer 2A (Figure 8). Ewan may correspond instead to a minor axial upwelling relative  
431 the MLSHF, and associated with a downwelling area below the rifted axial volcano  
432 located between these two hydrothermal fields (Figure 3). Alternatively, Ewan may be  
433 associated with a recent magmatic event such as the emplacement of a lava flow or dike  
434 propagation in the shallow crust as suggested by hydrophone data (Dziak et al., 2004).

#### 435 *4.3 Revised hydrothermal heat flux at Lucky Strike*

436 The new observations and results presented here allow us to update the heat flux  
437 estimates of known hydrothermal activity at the Lucky Strike segment (Ewan and  
438 Capelinhos in addition to MLSHF), based on visual and instrumental observations. A  
439 prior estimate of heatflux for MLSHF, based on the photomosaic and a systematic  
440 evaluation of the distribution of vents, yielded values of 195-1086 MW (Barreyre et al.,  
441 2012). As the only new hydrothermal area within this field found in this study is inactive,  
442 this estimate remains unchanged.

443 Ewan displays only diffuse and low-temperature hydrothermal discharge, that we have  
444 fully mapped using the seafloor photomosaics (Figure 5). Adopting the methodology of  
445 Barreyre et al. (2012), we estimate the minimum and maximum heatflux based on the  
446 area of diffuse outflow estimated from the photomosaics (Figure 3), and the estimated  
447 temperature and velocity of the outflow from studies in similar settings (see details in  
448 Barreyre et al., 2012, and Table 2). We obtain a heatflux estimate that ranges from 4.4-  
449 117 MW. In our calculations we likely underestimate the surface of diffuse outflow, as it  
450 is calculated over images projected to a horizontal plane without taking into account the  
451 steep topography present in the area (Figure 5). As in the case of the MLSHF diffuse  
452 fluxes, other uncertainties are the velocity and the temperature of the diffuse outflow,  
453 which are not constrained by systematic measurements at this site. Visual inspection of  
454 the Capelinhos site shows that there are two active main chimneys with a total of ~10-  
455 15 vents identified (Figure 4), in addition to flanges with diffusers. Assuming a total of  
456 10-20 vents with a heatflux of 0.12-0.8 MW/vent (Barreyre et al., 2012; Mittelstaedt et al.,  
457 2012) we estimate the Capelinhos heat-flux at 1.2-16 MW.

458 The hydrothermal heat flux that we estimate for the new active sites (5.6-133 MW, Table  
459 2) are thus minor relative to the 195/1086 MW previously reported for the MLSHF

460 (Barreyre et al., 2012). This represents an increase of ~10% in our heatflux estimate  
461 that is taken up primarily by diffuse hydrothermal outflow (80-90% of the total heatflux,  
462 Table 2), although the importance of diffuse outflow appears to vary greatly from site to  
463 site (100% at Ewan and almost non-existent at Capelinhos).

#### 464 *4.4 Water column anomalies and elusive hydrothermal plumes*

465 Water column studies throughout the Lucky Strike segment report anomalies attributed  
466 to hydrothermal plumes rising from undiscovered fields, although their evidence is  
467 elusive. Light transmission anomalies and elevated CH<sub>4</sub> concentrations south of the  
468 MLSHF and central volcano (Wilson et al., 1996) have been attributed to an unidentified  
469 but large field at ~2100 m (W in Figure 9). During the HEAT cruise (German et al., 1996),  
470 TOBI deep-tow sonar detected one anomaly along the non-transform offset between  
471 Lucky Strike North and Famous segments, and another one at the southern edge of the  
472 nodal basin during a hydrographic cast (G in Figure 9). More recently, hydrographic  
473 stations revealed a water column anomaly at 1800 m bsl at the southern segment  
474 end (Thurnherr et al., 2008) (T in Figure 9). Finally, CH<sub>4</sub> anomalies indicating low-  
475 temperature hydrothermal activity associated with serpentinization and not linked to  
476 black smoker activity (lack of a manganese signature) have been identified at Menez  
477 Hom (Gràcia et al., 2000), and at the southern inside-corner of the Lucky Strike  
478 segment (Gr in Figure 9).

479 Numerous other hydrographic profiles conducted throughout this segment show no  
480 water column anomaly. These including casts during the Gravituck cruise shown in  
481 Figure 9 (Thurnherr et al., 2008), ROV dives during the cruises in 2008 and 2009 (Figure  
482 9 and Supplementary Table 1), or deep-towed surveys using TOBI (German et al., 1996;  
483 Gràcia et al., 1998), which detected no water column anomalies other than those along  
484 the non-transform offset and the end of the segment (German et al., 1996) (Figure 9). In  
485 many casts, the plume of the MLSHF is not detected (Figure 9), likely due to complex  
486 hydrography and strong seafloor currents (Thurnherr et al., 2008) that may sweep or  
487 dilute its plume. Furthermore, seafloor observations and microbathymetry surveys  
488 available in the immediate proximity of some of these anomalies (Figure 9) provide no  
489 evidence of activity away from the three active hydrothermal fields at the center of the  
490 segment (Figure 3). Therefore the evidence for additional undiscovered hydrothermal  
491 fields inferred along the southern portion of the Lucky Strike segment (Wilson et al.,  
492 1996; German et al., 1996; Thurnherr et al., 2008) is weak owing to the unexplained  
493 spatial and temporal inconsistencies of hydrographic data indicating the presence or

494 absence of hydrothermal plumes, the lack of visual or morphologic indicators of  
495 hydrothermal activity away from the segment center, and the complex hydrography of  
496 the area.

#### 497 *4.5. Significance for hydrothermal activity along slow spreading segments*

498 Central volcanoes other than Lucky Strike host active vents. At intermediate-spreading  
499 ridges, Axial Volcano along the Juan de Fuca Ridge is also underlain by a magma  
500 chamber 2.5-3.5 km below seafloor, hosts several hydrothermal sites that are  
501 monitored (Kelley et al., 2014). At slower-spreading ridges, the Menez Gwen  
502 field (Ondreas et al., 1997; Marcon et al., 2013) and the Koberinsey field (Olafsson et al.,  
503 1989) along the Mid-Atlantic Ridge, and the Soria Moria and Troll Wall along the Arctic  
504 Ridges (Pedersen et al., 2010) all occur on central volcanoes at similar phases of rifting as  
505 that of Lucky Strike, dissected at the summit by narrow and localized axial graben. It is  
506 likely that these sites are also underlain by magma chambers linked to central volcano  
507 formation, and such fields may be common at central volcanoes along ridge segments  
508 (Escartín et al., 2014) that are yet unexplored.

509 Hydrothermal activity at central volcanoes is likely to be persistent over long periods of  
510 time, continuously or intermittently, owing to sustained and enhanced melt supply  
511 required for their formation. This is supported by the presence of both isolated  
512 hydrothermal vents and areas of hydrothermal deposits that are inactive at Lucky Strike  
513 (Area 5, Table 1), and by the off-axis Grunnus site on a rifted central volcano. While  
514 there are no age constraints on hydrothermal deposits at the Main Lucky Strike  
515 hydrothermal field (Figure 3), it is likely to have been active over thousands to a few tens  
516 of thousands of years (Humphris et al., 2002; Barreyre et al., 2012). Other basalt-hosted  
517 hydrothermal fields found along axial volcanic ridges (e.g., Broken Spur (Murton et al.,  
518 1994; Murton et al., 1999), Snake Pit (Karson and Brown, 1988), BeeBee (Connelly et al.,  
519 2012) or Lilliput (Haase et al., 2009)) are much smaller in size and probably with  
520 shorter life-spans. These may be likely associated to short-lived heat sources (e.g., dike  
521 intrusions or recent volcanic eruptions). The long-lived hydrothermal fields  
522 associated with central volcanoes are likely to play a major role in the dispersion and  
523 propagation along the ridge-axis of hydrothermal ecosystems and on the biogeography  
524 of these communities (Van Dover et al., 2002).

## 525 **Conclusions**



526 Extensive seafloor imagery and visual observations together with microbathymetry  
527 acquired with deep-sea vehicles have allowed us to evaluate the distribution of  
528 hydrothermal activity at the scale of the Lucky Strike segment, and to re-evaluate the  
529 associated heatflux. The Lucky Strike segment hosts three active hydrothermal fields:  
530 The known MLSHF, Capelinhos, and Ewan. Capelinhos is located 1.3 km E of the axis and  
531 the Main field, and consists of a ~20 m sulfide mound with black smoker vents. Ewan is  
532 located ~1.8 km south from the Main LS field long the axial graben, and displays only  
533 diffuse flow along and around scarps of collapse structures associated with fault scarps.  
534 At the Main Lucky Strike hydrothermal field we have identified an inactive site, thus  
535 broadening the extent of this field. Heat flux estimates from these new sites are relatively  
536 low and correspond to ~10% of the heat flux estimated for the Main field, with an  
537 integrated heatflux of 200-1200 MW. Overall, most of the flux (up to 80-90%) is  
538 associated with diffuse flow, with the Ewan site showing solely diffuse flow and  
539 Capelinhos mostly focused flow. The microbathymetry also reveals a large, off-axis (~2.4  
540 km) hydrothermal field, comparable to the TAG mound in size, on the flanks of a rifted  
541 volcano. The association of these fields to a central volcano, and the absence of  
542 indicators of hydrothermal activity along the ridge segment, suggest that sustained  
543 hydrothermal activity is maintained by the enhanced melt supply and the associated  
544 magma chamber(s) required to build central volcanoes. In all cases hydrothermal  
545 outflow at the seafloor is controlled by faults, indicating that these tectonic structures  
546 are permeable and exploited by the hydrothermal circulation in the shallow crust. Our  
547 observations, together with inconsistencies in available oceanographic data, also fail to  
548 constrain the possible source(s) of all anomalies detected in water column. Central  
549 volcanoes are thus associated with long-lived hydrothermal activity, and these sites may  
550 play a major role in the distribution and biogeography of vent communities.

551

552

553 **Acknowledgements.** This work has been partly financed by ANR (France) Mothseim  
554 Project NT05-3 42213 to JE, and by EU-RTN-MOMARNET to MC. The French Ministry of  
555 Research financed ship, ROV and AUV time (Graviluck'06, MOMAR'08, Bathyluck'09,  
556 MOMARSAT cruises in 2010-2015). *TowCam* deployment during Graviluck cruise was  
557 supported by NSF grant OCE-0623744 to A. Soule and D. J. Fornari (WHOI, USA).

558 **Table 1.** Hydrothermal fields at the Lucky Strike ridge segment. The limit of sites H1 through H4 in the Main Lucky Strike field have been  
 559 defined previously (Ondréas et al., 2009), as well the distribution of focused and diffuse hydrothermal outflow by (Barreyre et al., 2012). Sites  
 560 H5 and H6 in the Main Lucky Strike Field, and the Ewan, Capelinhos, and Grunnus fields are described in this paper.  
 561

<i>Name</i>	<i>Longitude</i>	<i>Latitude</i>	<i>Depth, m</i>	<i>Area, m<sup>2</sup></i>	<i>Distance, km (spreading age, kyr)<sup>#</sup></i>	<i>In situ data</i>	<i>Activity*</i>
<b>Main Lucky Strike field</b>					0-0.6 (0-53)	Visual, photomosaic	
H1	32°16.92'W	37°17.61'N	1620-1720	30304			Active, f+d
H2	32°16.50'W	37°17.48'N	1620-1670	35535			Active, f+d
H3-Eiffel Tower	32°16.52'W	37°17.33'N	1680	1506			Active, f+d
H3a	32°16.60'W	37°17.43'N	1670	5066			Active, f+d
H3b	32°16.62'W	37°17.37'N	1680-1700	3856			Active, f+d
H3c	32°16.52'W	37°17.27'N	1700	1454			Active, f+d
H4	32°16.90'W	37°17.41'N	1710	282			Active, f+d
H5	32°16.84'W	37°17.39'N	1725	10429			Active, f+d
H6a	32°17.08'W	37°17.71'N	1585	4479			Inactive
H6b	32°17.05'W	37°17.64'N	1590	2259			Inactive
H6c	32°17.07'W	37°17.69'N	1590	2597			Inactive
<b>Ewan</b>	32°17.27'W	37°16.61'N	1770	3010	0 (0)	Visual, photomosaic	Active, d
<b>Capelinhos</b>	32°15.83'W	37°17.35'N	1665	20712	1.4 (130)	Visual	Active, f (d)
<b>Grunnus</b>	32°18.25'W	37°18.02'N	1645	35704	2.4 (220)	None	Inactive?

584 Notes:#Distance is measured to centerline of axial graben, and spreading age calculated assuming a full spreading rate of 22 km/Myr. For the main  
 585 Lucky Strike we report the minimum and maximum distances and the associated spreading ages.

586 \*Activity of sites is confirmed visually except for Grunnus, which has not been visited to date. Type of flow: f - focused flow (vents); d - diffuse flow.  
 587 Type of flow in parenthesis denotes minor occurrence.

588 **Table 2.** Ranges (min/max)? Heatflux estimates of Lucky Strike hydrothermal fields.  
 589 Calculations are based on the number of high-temperature vents and surface of areas of  
 590 diffuse flow identified visually (this study) and instrumental measurements (temperature,  
 591 currents), following the methodology of Barreyre et al. (2012).

592 Ewan hydrothermal field (diffuse)

593	Large patches:	S: 274 m <sup>2</sup>	Q=4.2/92 MW
594	Small matches:	Number=1072; S: 11 m <sup>2</sup>	Q=0.2/15 MW
595	Total EWAN		Q=4.4/117 MW

597 Capelinhos hydrothermal field (focused)

598	Vents	Number= 10-20; Q/vent=0.12-0.8 MW	Q=1.2/16 MW
-----	-------	-----------------------------------	-------------

600 Main Lucky Strike hydrothermal field (focused + diffuse)(Barreyre et al., 2012)

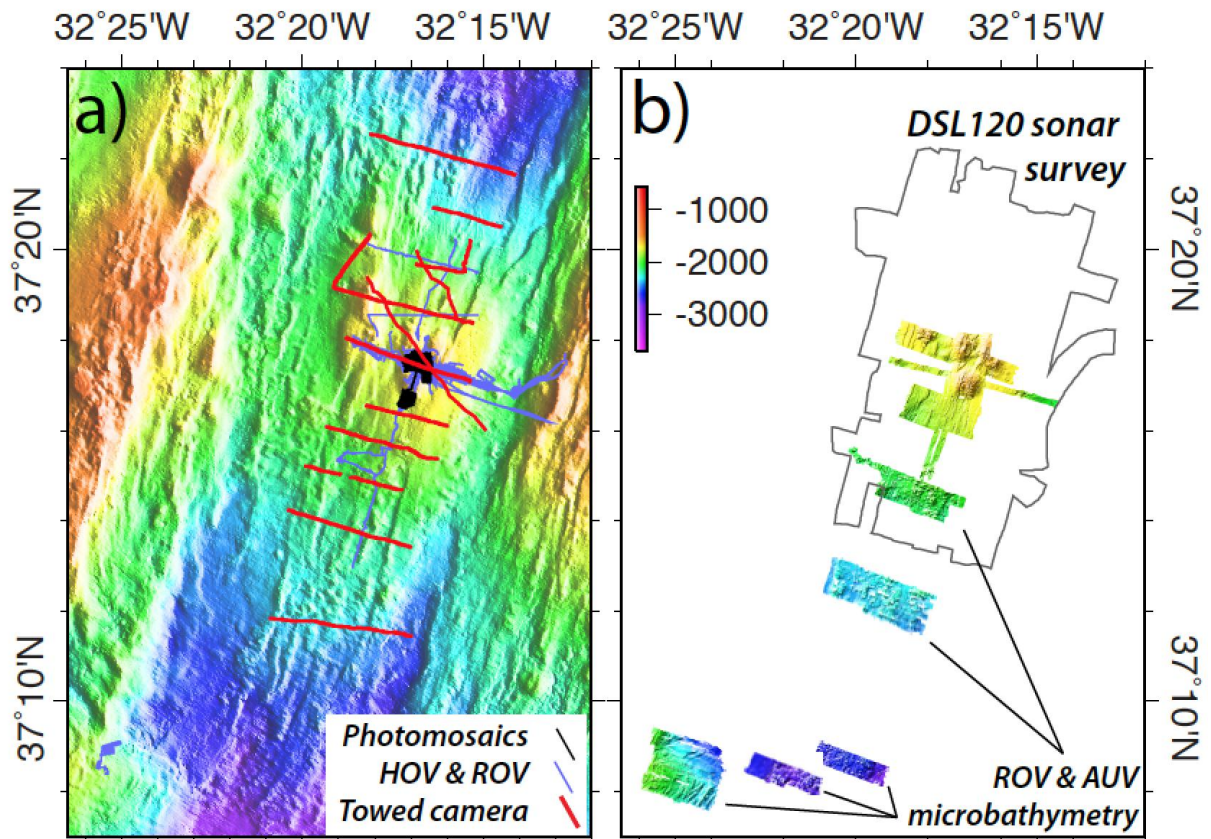
601	Diffuse flow		Q=187/1036 MW
602	Focused flow		Q=8/50 MW
603	Total MLSHF		Q=195/1086 MW

605 Combined heat-fluxes at Lucky Strike

606	<b>Diffuse flow</b>		<b>Q=191/1143 MW</b>
607	<b>Focused flow</b>		<b>Q=9/66 MW</b>
608	<b>Total heatflux</b>		<b>Q=200/1210 MW</b>

609 \* Diffuse flow:  $Q = \Delta T \times \phi \times v \times C_p \times S$ , where  $f$  is density of seawater (1025 kg.m<sup>-3</sup>),  $C_p$  is the  
 610 specific heat of the diffuse fluid (4.2 10<sup>3</sup> J.kg<sup>-1</sup>°C<sup>-1</sup>),  $\Delta T$  is temperature difference  $T-T_0$  between  
 611 outflow temperature  $T$  and ambient seawater  $T_0$  (4.4°C),  $v$  is the diffuse effluent velocity, and  $S$   
 612 the area of considered diffuse outflow (m<sup>2</sup>).  $T$  minimum and maximum values are 8 and 20°C,  
 613 and  $V$  minimum and maximum values are 1 and 5 mm/s, as described by Barreyre et al. (2012)  
 614 and references therein.  $S$  is reported in the Table 1.

615 Focused flow: Individual vent heatflux is estimated at 0.12-8 MW, as described by Barreyre  
 616 et al. (2012). The total heatflux associated to focused flow is the integration of the heatflux from  
 617 individual vents, which are visually identified in available ROV video imagery.

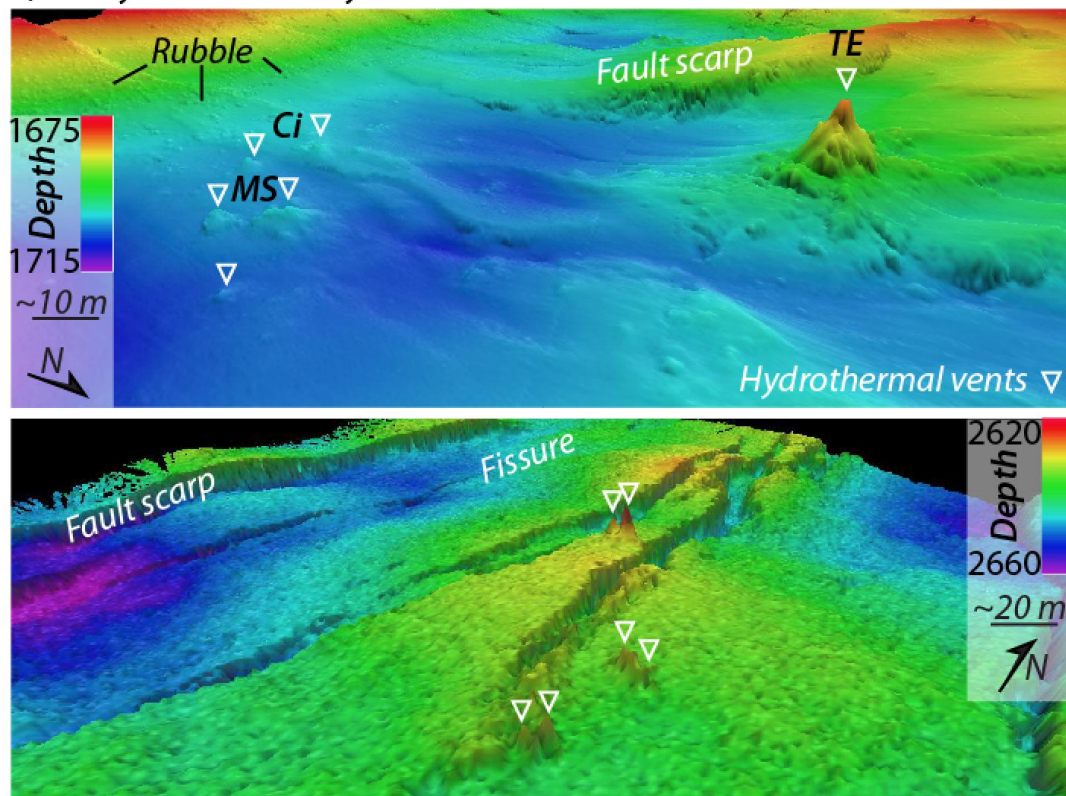


618

619

620 **Figure 1.** a) Visual information of the seafloor is available from ROV photomosaics, and  
 621 along tracks of HOVs, ROVs, and deep-towed cameras. b) Available microbathymetric  
 622 data from the Lucky Strike ridge segment, acquired during near-bottom ROV and AUV  
 623 surveys (Momareto'06 and MOMAR'08 and Bathyluck'09 cruises). The outline of the  
 624 DSL120 sonar survey, acquired during the Lustre'96 cruise, is also shown. See  
 625 Supplementary Table 1 for additional details on these cruises, the deep-sea vehicles  
 626 deployed, and types of data acquired.

a) Lucky Strike Main Hydrothermal Field

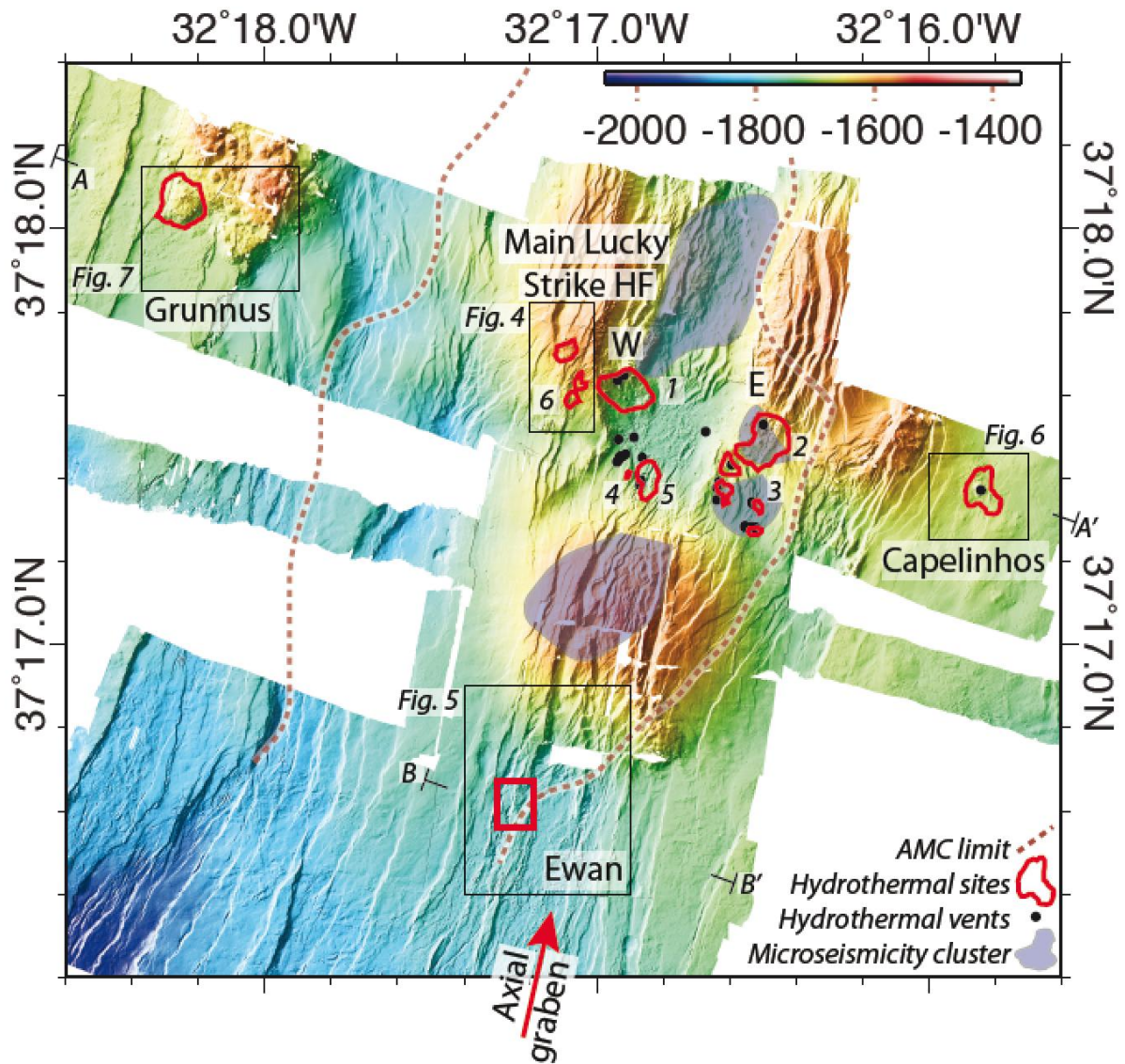


b) Kilo Moana Hydrothermal Field (Lau Basin)

627

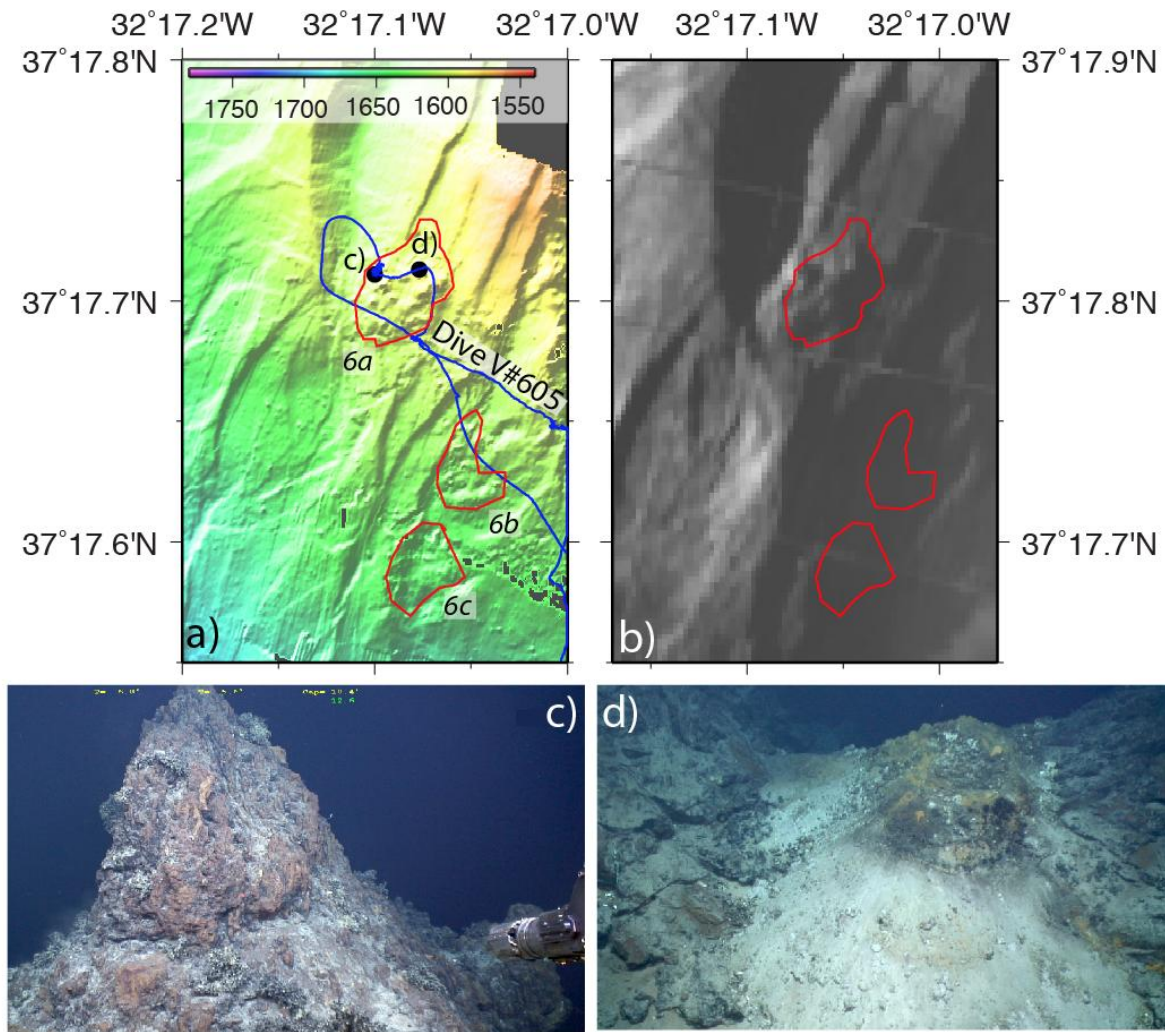
628 **Figure 2.** Perspective views showing the ‘lumpy’ seafloor morphology associated with  
629 hydrothermal deposits described in the text. a) Microbathymetry from the Lucky Strike  
630 Main Hydrothermal field, showing the ~20 m high Tour Eiffel (TE) vent and the  
631 associated hydrothermal deposits around it, and smaller nearby vents (MS: Montsegur;  
632 Ci: Cimendef). The view shows also several fault scarps and rubble on slopes, that are  
633 morphologically distinct from hydrothermal deposits. b) Microbathymetry showing  
634 hydrothermal vents in the Kilo Moana Hydrothermal Field in the Lau Basin (Ferrini et al.,  
635 2008; Ferrini and Tivey, 2012), rising ~10-20 m above surrounding seafloor that is  
636 faulted and fissured.





637

638 **Figure 3.** Microbathymetry of the Lucky Strike segment center showing the four  
 639 hydrothermal fields identified and the present-day zone of accretion along the axial  
 640 graben (red arrow). Red contours correspond to the limits of hydrothermal deposits  
 641 identified in the microbathymetry, which are numbered for the Main Lucky Strike Field.  
 642 The red square corresponds to the Ewan field, which lacks a geomorphologic signature,  
 643 and black dots correspond to active vents. Boxes indicate the location of Figures 4  
 644 through 7, and characteristics of fields are given in Table 1. The limits of the AMC (Singh  
 645 et al., 2006; Combier et al., 2015) and location of microseismicity clusters (Crawford et al.,  
 646 2013) are also shown. A-A' and B-B' indicate endpoints of profiles shown in Figure 8a.



647

648

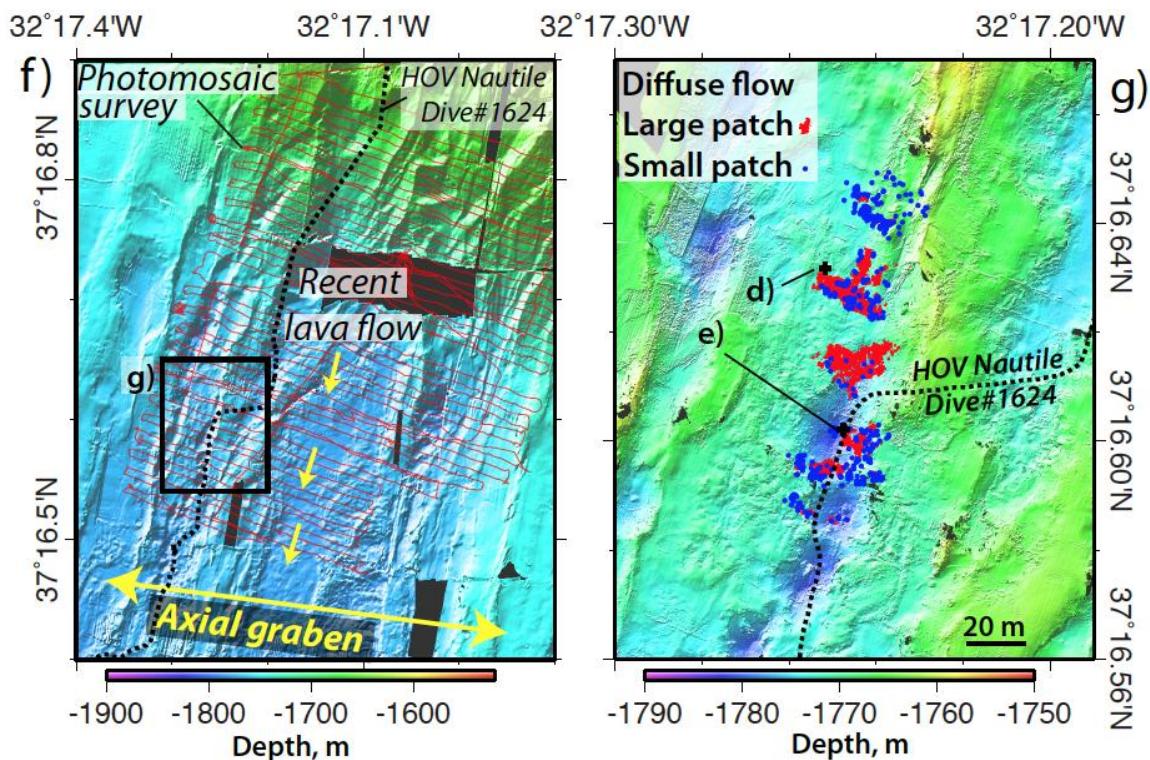
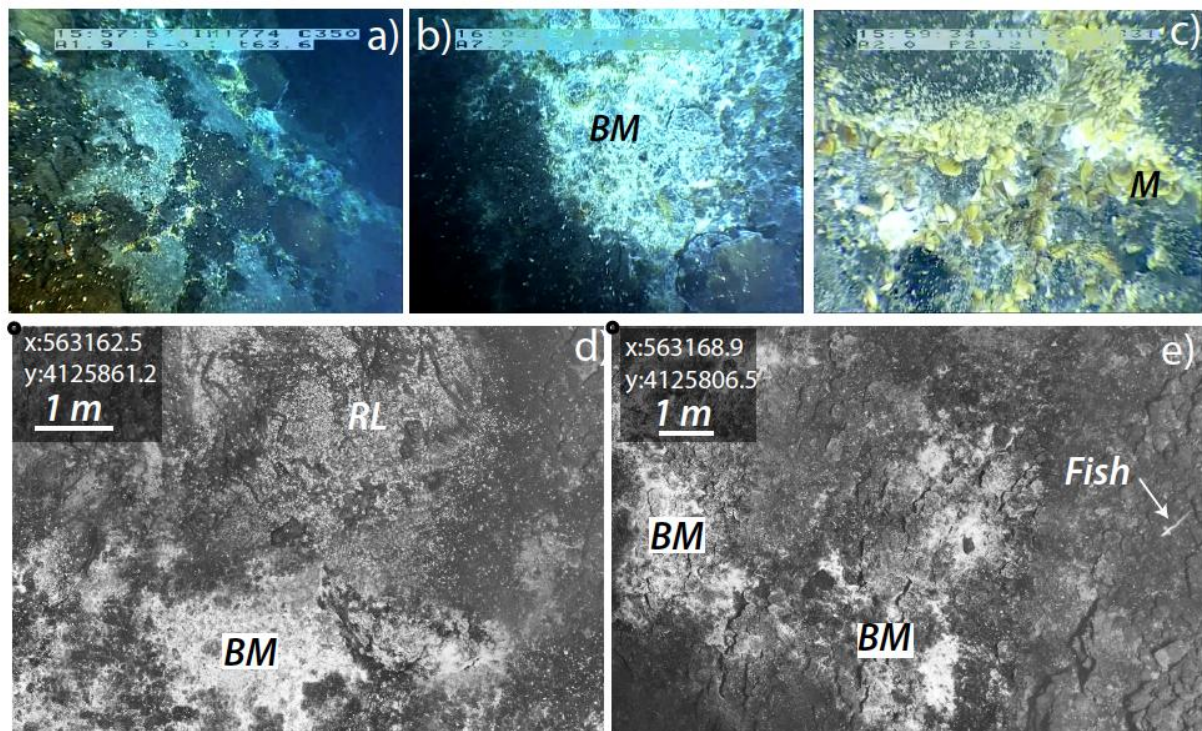
649 **Figure 4.** a) Microbathymetry of the western edge of the MLSHF, showing hydrothermal  
 650 areas 6a-c in red (see Table 1 and Figure 3). c) and d) indicate the location of photos in  
 651 Figures 4c and 4d, respectively. b) Acoustic backscatter image of the same area, with  
 652 insonification from the west. Bright areas correspond to high backscatter, and black to  
 653 acoustic shadows in this and following figures with sonar imagery. c) Inactive chimney  
 654 and d) hydrothermal mound associated deposits observed during ROV VICTOR dive  
 655 #605 (blue line).

656

657

658



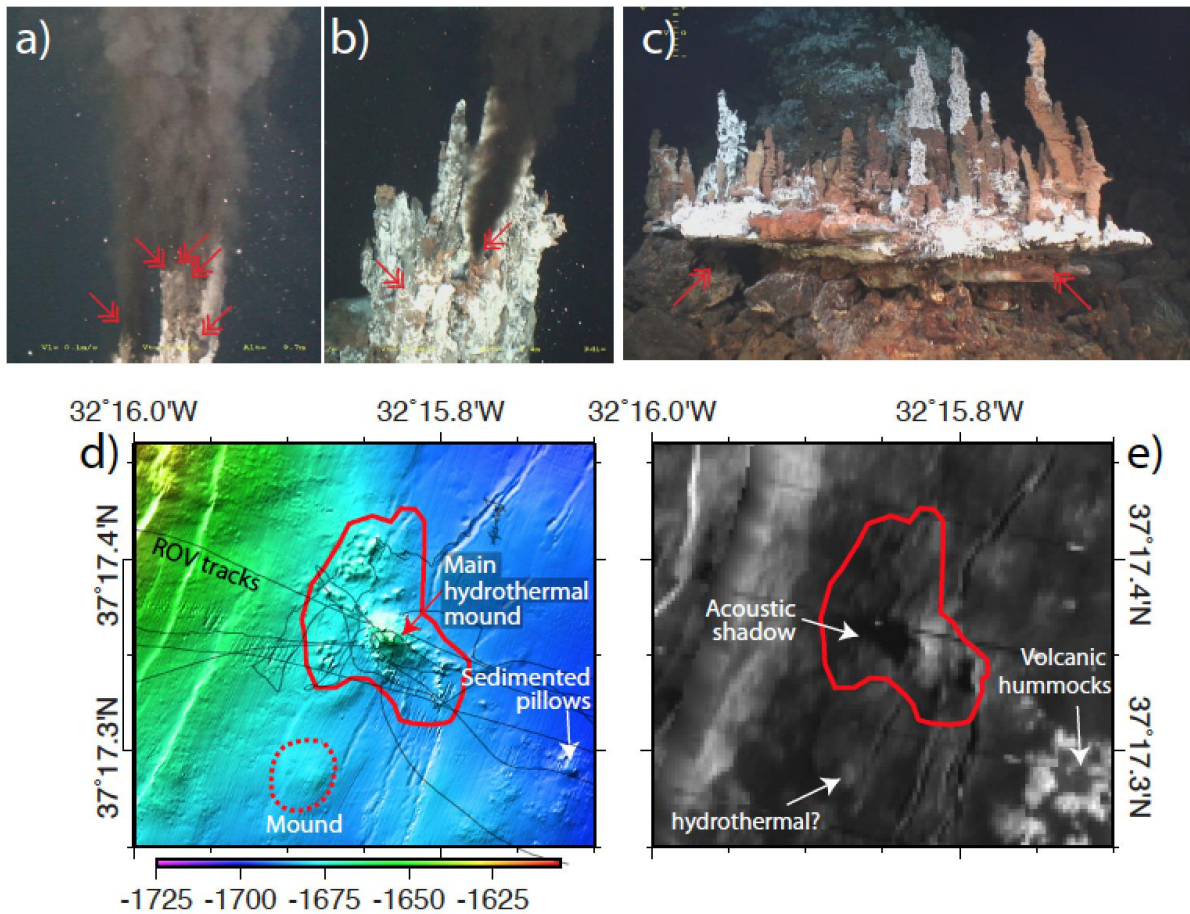


659

660 **Figure 5.** Ewan hydrothermal field. a)-c) Video grabs from HOV Nautilie dive #1616  
 661 (Graviluck'06) show hydrothermal activity along steep slopes (a), with irregular patches  
 662 of bacterial mats and diffuse flow through rubble (b), and associated with mussel beds  
 663 (c). d) Vertical seafloor image mosaics (Bathyluck'09) showing patches of bacterial mats  
 664 (BM) associated with diffuse flow extending over several meters over sedimented ropy  
 665 lava flows (RL). e) Irregular bacterial mat patches, indicating localized diffuse outflow  
 666 through steep scarps. Microbathymetry (50 cm/pixel) of the ridge axis on the southern  
 667 flank of the rifted seamount south of the Main Lucky Strike field (f) and detail of the  
 668 active zones (g). The coordinates of the top left corner of the photomosaics d) and e) are  
 669 in UTM (m), and located in g).

670

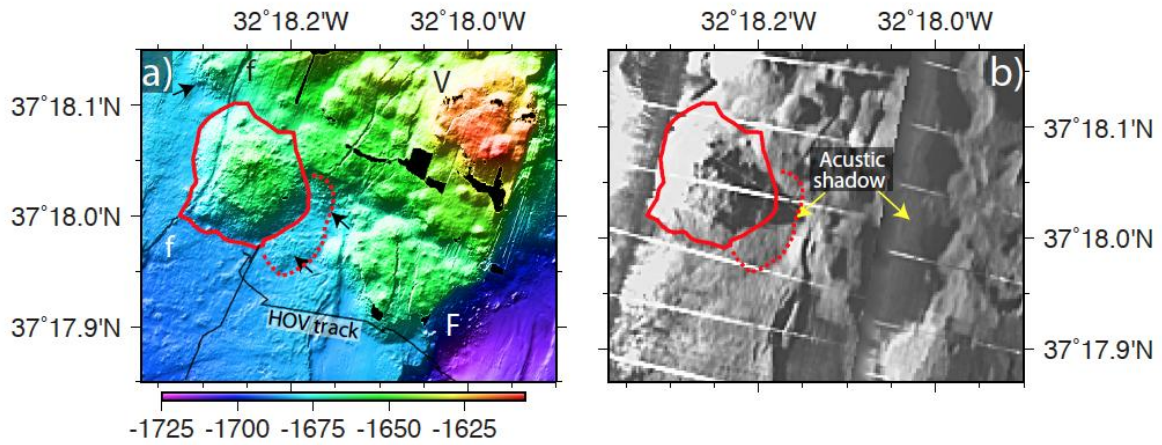




671

672 **Figure 6.** Capelinhos hydrothermal site. The main Capelinhos hydrothermal mound  
 673 shows active chimneys with several black smoker vents (a-b) flanges with diffusers (c).  
 674 Diffuse hydrothermal activity (bacterial mats) is scarce. d) Microbathymetry of the  
 675 Capelinhos hydrothermal field (red outline), which displays a ~20 m high edifice  
 676 emplaced over a set of small-scale faults and fissures, and a possible hydrothermal  
 677 mound to the south (not visually inspected). e) Acoustic backscatter image with  
 678 insonification from the E, showing the acoustic shadow of the edifice. The bathymetry  
 679 reveals several mounds in surrounding areas (arrows); the structure to the SW has low  
 680 acoustic backscatter and may correspond to another hydrothermal deposit. The  
 681 structures to the SE are instead acoustically reflective and the sonar texture corresponds  
 682 to volcanic hummocks.

683

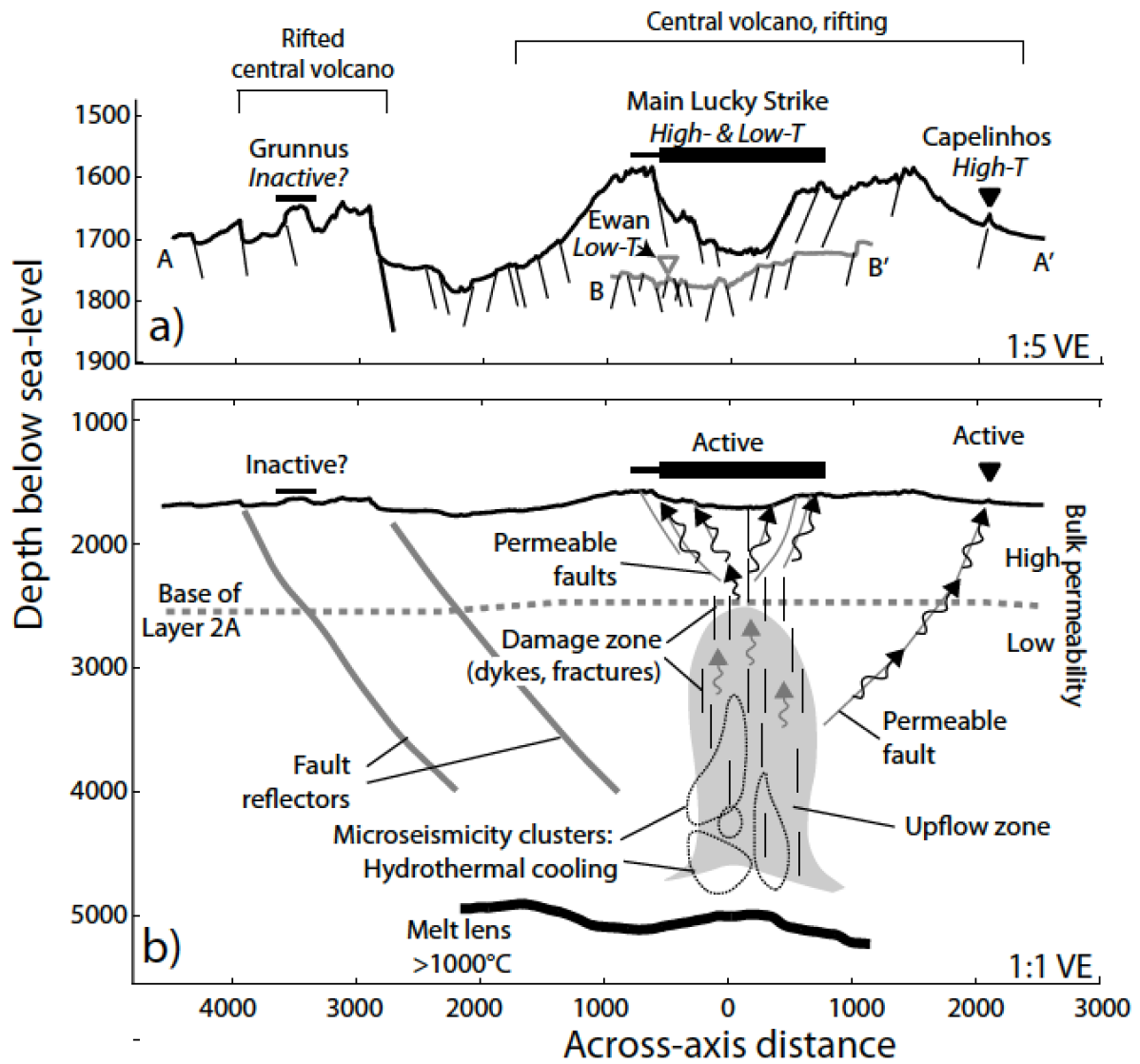


684

685

686 **Figure 7.** a) Microbathymetry of the Grunnus hydrothermal field (solid red line), and  
 687 other possible hydrothermal structures (black arrows, dashed red line) located on the  
 688 flank of a rifted central volcano (V, see Figure 3). A small normal fault (f) dissects the  
 689 western flank of the ~200 meter diameter mound, while major fault (F) that dissects the  
 690 central volcano can be linked to a fault seismic reflector to a depth of ~2 km below  
 691 seafloor (Smith et al., 2006; Combier et al., 2015). b) Corresponding sonar imagery of the  
 692 area.

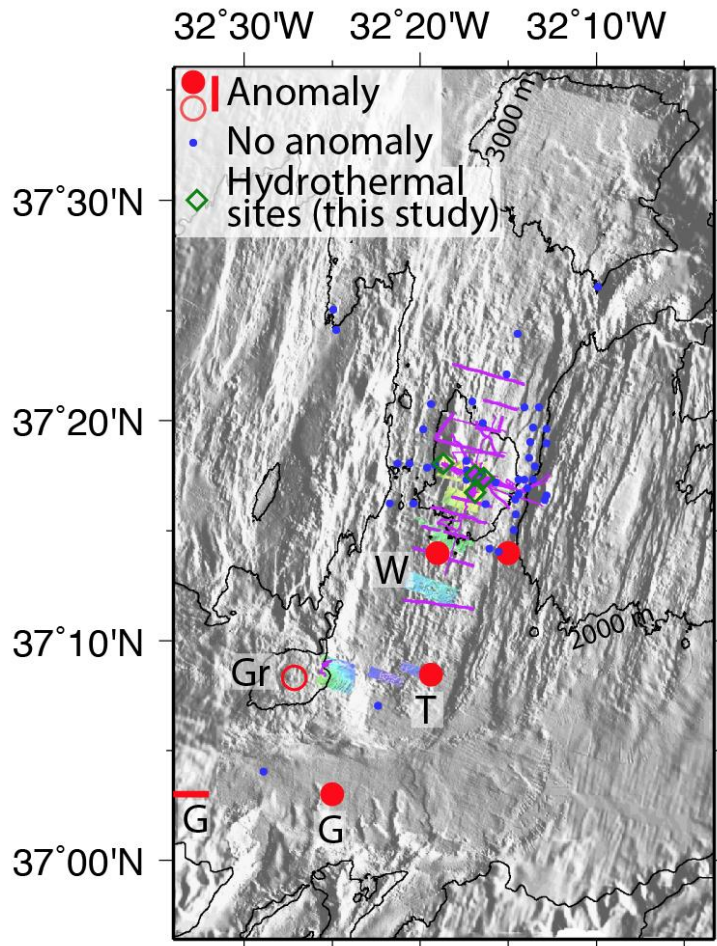
693



694

695 **Figure 8.** a) Microbathymetric profiles across the Grunnus-MLSHF-Capelinhos (black  
 696 line) and across Ewan (grey line, see Figure 3 for location). b) Vertical cross-axis  
 697 section of the crust showing the AMC and fault reflectors (Singh et al., 2006; Combiér et  
 698 al., 2015) and the base of Layer 2A (Seher et al., 2010) from seismic data, and the  
 699 projected positions of microseismicity clusters (Crawford et al., 2013). Hydrothermal  
 700 upflow below Layer 2A is likely diffuse in the form of upwellings up to ~1 km in  
 701 diameter (Fontaine et al., 2014) along the axis, which has a higher permeability due to  
 702 damage induced by diking and cracking (Fontaine et al., 2014; Escartín et al., 2014). In  
 703 the shallow crust hydrothermal outflow is likely channeled instead along permeable  
 704 faults.

705



706

707 **Figure 9.** Map of the Lucky Strike field showing the location of water column  
 708 nephelometry anomalies interpreted as indicators of hydrothermal plumes at depths of  
 709 ~1800 m bsl (red), and hydrographic casts conducted during the Graveluck2006 cruise  
 710 that yielded no anomalies (blue). Shaded relief is from shipboard bathymetry, the  
 711 purples lines correspond to to visual seafloor observations (Figure 1), the AUV and ROV  
 712 microbathymetry is shown in color (see Figure 3), and sites described in this paper  
 713 indicated by green diamonds. Water column anomalies: G: (German et al., 2006); T  
 714 (Thurnherr et al., 2008); W (Wilson et al., 1996); Gr(Gràcia et al., 2000).

715 **References**

- 716 Baker, E.T., 2007, Hydrothermal cooling of mid ocean ridge axes: Do measured and  
717 modeled heat fluxes agree? *Earth and Planetary Science Letters*, v. 263, p. 140–150.
- 718 Baker, E.T., Cormier, M.-H., Langmuir, C.H., and Zavala, K., 2001, Hydrothermal plumes  
719 along segments of contrasting magmatic influence, 15°20'–18°30'N, East Pacific  
720 Rise; Influence of axial faulting: *Geochemistry, Geophysics, Geosystems*, v. 2, p.  
721 2000GC000165.
- 722 Barreyre, T., Escartín, J., Garcia, R., Cannat, M., Mittelstaedt, E., and Prados, R., 2012,  
723 Structure, temporal evolution, and heat flux estimates from the Lucky Strike deep-  
724 sea hydrothermal field derived from seafloor image mosaics: *Geochemistry,  
725 Geophysics, Geosystems*, v. 13, no. 4, p. Q04007, doi: 10.1029/2011GC003990.
- 726 Barreyre, T., Escartin, J., Sohn, R., and Cannat, M., 2014a, Permeability of the Lucky Strike  
727 deep-sea hydrothermal system: Constraints from the poroelastic response to ocean  
728 tidal loading: *Earth and Planetary Science Letters*, v. 408, p. 146–154, doi:  
729 10.1016/j.epsl.2014.09.049.
- 730 Barreyre, T., Escartín, J., Sohn, R.A., Cannat, M., Ballu, V., and Crawford, W.C., 2014b,  
731 Temporal variability and tidal modulation of hydrothermal exit-fluid temperatures  
732 at the Lucky Strike deep-sea vent field, Mid-Atlantic Ridge: *Journal of Geophysical  
733 Research: Solid Earth*, v. 119, no. 4, p. 2543–2566, doi: 10.1002/2013JB010478.
- 734 Bischoff, J.L., and Seyfried, W.E., 1978, Hydrothermal chemistry of seawater from 25° to  
735 350°C: *American Journal of Science*, v. 278, p. 838–860.
- 736 Bougault, H., Charlow, J.-L., Fouquet, Y., Needham, H.D., Vaslet, N., Appriou, P., Jean  
737 Baptiste, P., Rona, P.A., Dmitriev, L., and Silantiev, S., 1993, Fast and slow-spreading  
738 ridges: Structure and hydrothermal activity, ultramaphic topographic highs, and  
739 CH<sub>4</sub> output: *Journal of Geophysical Research*, v. 98, no. B6, p. 9643–9651.
- 740 Charlou, J.-L., and Donval, J.-P., 1993, Hydrothermal methane venting between 12°N and  
741 26°N along the Mid-Atlantic ridge: *Journal of Geophysical Research*, v. 98, no. B6, p.  
742 9625–9642.
- 743 Colaço, A., Blandin, J., Cannat, M., Carval, T., Chavagnac, V., Connelly, D., Fabian, M.,  
744 Ghiron, S., Goslin, J., Miranda, J.M., Reverdin, G., Sarrazin, J., Waldmann, C., and  
745 Sarradin, P.-M., 2011, MoMAR-D: a technological challenge to monitor the dynamics  
746 of the Lucky Strike vent ecosystem: *ICES Journal of Marine Science*, v. 68, no. 2, p.  
747 416–424. doi:10.1093/icesjms/fsq075.
- 748 Combier, V., Seher, T., Singh, S.C., Crawford, W.C., Cannat, M., Escartín, J., and Dusunur, D.,  
749 2015, Three-dimensional geometry of axial magma chamber roof and faults at  
750 Lucky Strike volcano on the Mid-Atlantic Ridge: *Journal of Geophysical Research:  
751 Solid Earth*, p. n/a–n/a, doi: 10.1002/2015JB012365.
- 752 Connelly, D.P., Copley, J.T., Murton, B.J., Stansfield, K., Tyler, P. a, German, C.R., Van Dover,  
753 C.L., Amon, D., Furlong, M., Grindlay, N., Hayman, N., Hühnerbach, V., Judge, M., Le  
754 Bas, T., et al., 2012, Hydrothermal vent fields and chemosynthetic biota on the  
755 world's deepest seafloor spreading centre.: *Nature communications*, v. 3, p. 620,  
756 doi: 10.1038/ncomms1636.



- 757 Crawford, W.C., Rai, A., Singh, S.C., Cannat, M., Escartín, J., Wang, H., Daniel, R., and  
758 Combier, V., 2013, Hydrothermal seismicity beneath the summit of Lucky Strike  
759 volcano, Mid-Atlantic Ridge: *Earth and Planetary Science Letters*, v. 373, p. 118–  
760 128.
- 761 Crawford, W.C., Singh, S.C., Seher, T., Combier, V., Dusunur, D., Cannat, M., Rona, P.,  
762 Devey, C.W., Dymont, J., and Murton, B., 2010, Crustal structure, magma chamber  
763 and faulting beneath the Lucky Strike hydrothermal fields, *in* Diversity of  
764 Hydrothermal Systems on Slow Spreading Ocean Ridges, AGU, Washington DC, p.  
765 113–132.
- 766 Van Dover, C.L., German, C.R., Speer, K.G., Parson, L.M., and Vrijenhoek, R.C., 2002,  
767 Evolution and Biogeography of Deep-Sea Vent and Seep Invertebrates: *Science*, v.  
768 295, p. 1253–1257.
- 769 Dziak, R.P., Smith, D.K., Bohnenstiehl, D.R., Fox, C.G., Desbruyères, D., Matsumoto, H.,  
770 Tolstoy, M., and Fornari, D.J., 2004, Evidence of a recent magma dike intrusion at the  
771 slow spreading Lucky Strike segment, Mid-Atlantic Ridge: *Journal of Geophysical*  
772 *Research*, v. 109, p. B12102, doi: 10.1029/2004JB003141.
- 773 Escartín, J., García, R., Delaunoy, O., Ferrer, J., Gracias, N., Elibol, A., Cufi, X., Fornari, D.J.,  
774 Humphris, S.E., and Renard, J., 2008, Globally-aligned photo mosaic of the Lucky  
775 Strike hydrothermal Vent Field (Mid-Atlantic Ridge, 37°18.5'N): release of geo-  
776 referenced data, mosaic construction and viewing software: *Geochemistry,*  
777 *Geophysics, Geosystems*, v. 9, no. 12, p. Q12009, doi:10.1029/2008GC002204.
- 778 Escartin, J., Garcia, R., Delaunoy, O., Ferrer, J., Gracias, N., Elibol, A., Cufi, X., Neumann, L.,  
779 Fornari, D.J., Humphris, S.E., and Renard, J., 2008, Globally aligned photomosaic of  
780 the Lucky Strike hydrothermal vent field (Mid-Atlantic Ridge, 37 degrees 18.50 ` N):  
781 Release of georeferenced data, mosaic construction, and viewing software:  
782 *GEOCHEMISTRY GEOPHYSICS GEOSYSTEMS*, v. 9, doi: 10.1029/2008GC002204.
- 783 Escartín, J., Soule, S.A., Cannat, M., Fornari, D.J., Düşünür, D., and Garcia, R., 2014, Lucky  
784 Strike seamount: Implications for the emplacement and rifting of segment-centered  
785 volcanoes at slow spreading mid-ocean ridges: *Geochemistry, Geophysics,*  
786 *Geosystems*, v. 15, no. 11, p. 4157–4179, doi: 10.1002/2014GC005477.
- 787 Ferrini, V., and Tivey, M.K., 2012, ROV Jason 2 near-bottom multibeam bathymetry grids  
788 from 6 vent fields in the Lau Back-arc Basin: *Integrated Earth Data Applications*  
789 (IEDA), p. <http://doi.org/10.1594/IEDA/100028>.
- 790 Ferrini, V.L., Tivey, M.A., Carbotte, S.M., Martinez, F., and Roman, C., 2008, Variable  
791 morphologic expression of volcanic, tectonic, and hydrothermal processes at six  
792 hydrothermal vent fields in the Lau back-arc basin: *Geochemistry, Geophysics,*  
793 *Geosystems*, v. 9, no. 7, p. Q07022, doi:10.1029/2008GC002047.
- 794 Fontaine, F.J., Cannat, M., Escartin, J., and Crawford, W.C., 2014, Along-axis hydrothermal  
795 flow at the axis of slow spreading Mid-Ocean Ridges: Insights from numerical  
796 models of the Lucky Strike vent field (MAR): *Geochemistry, Geophysics,*  
797 *Geosystems*, v. 15, no. 7, p. 2918–2931, doi: 10.1002/2014GC005372.
- 798 Fontaine, F.J., Olive, J.A., Cannat, M., Escartin, J., and Perol, T., 2011,  
799 Hydrothermally-induced melt lens cooling and segmentation along the axis of fast-

- 800 and intermediate-spreading centers: *Geophysical Research Letters*, v. 38, p. L14307,  
801 doi:10.1029/2011GL047798.
- 802 Fouquet, Y., Charlou, J.L., Costa, I., Donval, J.P., Radford-Knoery, J., Pellé, H., Ondréas, H.,  
803 Lourenço, N., Ségonzac, M., and Tivey, M.K., 1994, A detailed study of the Lucky  
804 Strike hydrothermal site and discovery of a new hydrothermal site: Menez Gwen;  
805 Preliminary results of the DIVAI Cruise (5-29 May, 1994): *InterRidge News*, v. 3, no.  
806 2, p. 14–17.
- 807 German, C.R., Baker, E.T., Connelly, D.P., Lupton, J.E., Resing, J., Prien, R.D., Walker, S.L.,  
808 Edmonds, H.N., and Langmuir, C., 2006, Hydrothermal exploration of the Fonualei  
809 Rift and Spreading center and the Northeast Lau spreading center: *Geochemistry,*  
810 *Geophysics, Geosystems*, v. 7, no. 11, p. Q11022, doi:10.1029/2006GC001324.
- 811 German, C.R., Parson, L.M., and Team, H.S., 1996, Hydrothermal exploration near the  
812 Azores Triple Junction: tectonic control of venting at slow-spreading ridges: *Earth*  
813 *and Planetary Science Letters*, v. 138, p. 93–104.
- 814 German, C.R., Thurnherr, A.M., Knoery, J., Charlou, J.L., Jean Baptiste, P., and Edmonds,  
815 H.N., 2010, Heat, volume and chemical fluxes from submarine venting: A synthesis  
816 of results from the Rainbow hydrothermal field, 361N MAR: *Deep-Sea Research I*, v.  
817 57, p. 518–527.
- 818 Gràcia, E., Charlou, J.L., Radford-Knoery, J.R., and Parson, L.M., 2000, Non-transform  
819 offsets along the Mid-Atlantic Ridge south of the Azores (38°N–34°N): Ultramafic  
820 exposures and hosting of hydrothermal vents: *Earth and Planetary Science Letters*,  
821 v. 177, p. 89–103.
- 822 Gràcia, E., Parson, L.M., Bideau, D., and Hekinian, R., 1998, Volcano-tectonic variability  
823 along segments of the Mid-Atlantic Ridge between the Azores platform and Hayes  
824 fracture zone: Evidence from submersible and high-resolution side-scan sonar data,  
825 *in* Mills, R.A. and Harrison, K. eds., *Modern ocean floor processes and the geological*  
826 *record*, Geological Society, London, p. 1–15.
- 827 Haase, K.M., Koschinsky, A., Petersen, T., Devey, C.W., German, C., Lackschewitz, K.S.,  
828 Melchert, B., Seifert, R., Borowski, C., Giere, O., and Paulick, H., 2009, Diking, young  
829 volcanism and diffuse hydrothermal activity on the southern Mid-Atlantic Ridge:  
830 The Lilliput field at 9°33'S: *Marine Geology*, v. 266, p. 52–64.
- 831 Haymon, R.M., Macdonald, K.C., Benjamin, S.B., and Ehrhardt, C.J., 2005, Manifestations of  
832 hydrothermal discharge from young abyssal hills on the fast-spreading East Pacific  
833 Rise flank: *Geology*, v. 33, p. 153–156; doi: 10.1130/G21058.1.
- 834 Humphris, S.E., Fornari, D.J., Scheirer, D.S., German, C.R., and Parson, L.M., 2002,  
835 Geotectonic setting of hydrothermal activity on the summit of Lucky Strike  
836 seamount (37°17'N, Mid-Atlantic Ridge): *Geochemistry, Geophysics, Geosystems*, v.  
837 3, no. 8, p. 10.1029/2001GC000284.
- 838 Humphris, S.E., and Kleinrock, M.C., 1996, Detailed morphology of the TAG active  
839 hydrothermal mound: Insights into its formation and growth: *Geophysical Research*  
840 *Letters*, v. 23, no. 23, p. 3443–3446.

- 841 Jamieson, J.W., Clague, D. a., and Hannington, M.D., 2014, Hydrothermal sulfide  
842 accumulation along the Endeavour Segment, Juan de Fuca Ridge: *Earth and*  
843 *Planetary Science Letters*, v. 395, p. 136–148, doi: 10.1016/j.epsl.2014.03.035.
- 844 Karson, J.A., and Brown, J.R., 1988, Geologic setting of the Snake Pit hydrothermal site:  
845 an active vent field on the Mid-Atlantic Ridge: *Marine Geophysical Researches*, v. 10,  
846 p. 91–107.
- 847 Kelley, D.S., Delaney, J.R., and Juniper, S.K., 2014, Establishing a new era of submarine  
848 volcanic observatories: Cabling Axial Seamount and the Endeavour Segment of the  
849 Juan de Fuca Ridge: *Marine Geology*, v. 352, p. 426–450, doi:  
850 10.1016/j.margeo.2014.03.010.
- 851 Kleinrock, M.C., Humphris, S., and Thompson, G., 1993, Relations between volcanism,  
852 tectonism and hydrothermalism along the TAG segment of the Mid-Atlantic ridge:  
853 WHOI.
- 854 Klinkhammer, G., Rona, P., Greaves, M., and Elderfield, H., 1985, Hydrothermal  
855 manganese plumes in the Mid-Atlantic Ridge rift valley: *Nature*, v. 314, p. 727–731.
- 856 Lalou, C., Brichet, E., and Lange, J., 1989, Fossil hydrothermal sulfide deposits at the  
857 Galapagos Spreading Centre near 85°00 West: geological setting, mineralogy and  
858 chronology: *Oceanologica acta*, v. 12, no. 1, p. 1–8.
- 859 Langmuir, C., Humphris, S., Fornari, D., Van Dover, C., Von Damm, K., Tivey, M.K.,  
860 Colodner, D., Charlou, J. -l., Desonie, D., Wilson, C., Fouquet, Y., Klinkhammer, G., and  
861 Bougault, H., 1997, Hydrothermal vents near a mantle hot spot: the Lucky Strike  
862 vent field at 37°N on the Mid-Atlantic Ridge: *Earth and Planetary Science Letters*, v.  
863 148, p. 69–91.
- 864 Lupton, J., 1990, Water column hydrothermal plumes on the Juan de Fuca Ridge: *Journal*  
865 *of Geophysical Research*, v. 95, no. B8, p. 12829–12842.
- 866 Marcon, Y., Sahling, H., Borowski, C., dos Santos Ferreira, C., Thal, J., and Bohrmann, G.,  
867 2013, Megafaunal distribution and assessment of total methane and sulfide  
868 consumption by mussel beds at Menez Gwen hydrothermal vent, based on geo-  
869 referenced photomosaics: *Deep Sea Research Part I: Oceanographic Research*  
870 *Papers*, v. 75, p. 93–109, doi: 10.1016/j.dsr.2013.01.008.
- 871 Mittelstaedt, E., Escartín, J., Gracias, N., Olive, J.-A., Barreyre, T., Davaille, A., Cannat, M.,  
872 and Garcia, R., 2012, Quantifying diffuse and discrete venting at the Tour Eiffel vent  
873 site, Lucky Strike hydrothermal field: *Geochemistry Geophysics Geosystems*, v. 13,  
874 no. 4, p. Q04008, doi: 10.1029/2011GC003991.
- 875 Murton, B.J., Klinkhammer, G., Becker, K., Briais, A., Edge, D., Hayward, N., Millard, N.,  
876 Mitchell, I., Rousse, I., Rudnicki, J.W., Sayanagi, K., Sloan, H., and Parson, L., 1994,  
877 Direct evicence for the distribution and occurrence of hydrothermal activity  
878 between 27°N -30°N on the Mid-Atlantic Ridge: *Earth and Planetary Science Letters*,  
879 v. 125, p. 119–128.
- 880 Murton, B.J., Redbourn, L.J., German, C.R., and Baker, E.T., 1999, Sources and fluxes of  
881 hydrothermal heat, chemicals and biology within a segment of the Mid-Atlantic  
882 Ridge: *Earth and Planetary Science Letters*, v. 171, p. 301–317.



- 883 Olafsson, J., Honjo, S., Thors, K., Stefansson, U., Jones, R.R., and Ballard, R.D., 1989, Initial  
884 observations, bathymetry and photography of a geothermal site on the Kolbeinsey  
885 Ridge, *in* *Oceanography 1988* : JOA Mexico 88, p. 121–127.
- 886 Ondreas, H., Cannat, M., Fouquet, Y., Normand, A., Sarradin, P.M., and Sarrazin, J., 2009,  
887 Recent volcanic events and the distribution of hydrothermal venting at the Lucky  
888 Strike hydrothermal field, Mid-Atlantic Ridge: *GEOCHEMISTRY GEOPHYSICS*  
889 *GEOSYSTEMS*, v. 10, doi: 10.1029/2008GC002171.
- 890 Ondreas, H., Cannat, M., Fouquet, Y., Normand, A., Sarradin, P.-M., and Sarrazin, J., 2009,  
891 Recent volcanic events and the distribution of hydrothermal venting at the Lucky  
892 Strike hydrothermal field, Mid-Atlantic Ridge: *Geochemistry, Geophysics,*  
893 *Geosystems*, v. 10, no. 2, p. Q02006, doi:10.1029/2008GC002171.
- 894 Ondreas, H., Fouquet, Y., Voisset, M., and Radford-Knoery, J., 1997, Detailed study of  
895 three contiguous segments of the Mid-Atlantic Ridge, South of the Azores (37°N to  
896 38°30'N), using acoustic imaging coupled with submersible observations: *Marine*  
897 *Geophysical Researches*, v. 19, p. 231–255.
- 898 Pedersen, R.B., Thorseth, I.H., Nygård, T.E., Lilley, M., and Kelley, D.S., 2010,  
899 Hydrothermal Activity at the Arctic Mid-Ocean Ridges, *in* Rona, P., Devey, C.W.,  
900 Dymont, J., and Murton, B. eds., *Diversity of Hydrothermal Systems on Slow*  
901 *Spreading Ocean Ridges*, p. 67–89.
- 902 Prados, R., Garcia, R., Gracias, N., Escartín, J., and Neumann, L., 2012, A novel blending  
903 technique for underwater gigamosaicing: *IEEE Journal of Oceanic Engineering*, v.  
904 37, no. 4, p. 10.1109/JOE.2012.2204152.
- 905 Scheirer, D.S., Fornari, D.J., Humphris, S.E., and Lerner, S., 2000, High-resolution seafloor  
906 mapping using the DSL-120 sonar system: Quantitative assessment of sidescan and  
907 phase-bathymetry data from the Lucky Strike segment of the Mid-Atlantic Ridge:  
908 *Marine Geophysical Researches*, v. 21, p. 121–142.
- 909 Seher, T., Crawford, W.C., Singh, S.C., and Cannat, M., 2010, Seismic layer 2A variations in  
910 the Lucky Strike segment at the Mid-Atlantic Ridge from reflection measurements:  
911 *Journal of Geophysical Research*, v. 115, p. B07107, doi:10.1029/2009JB006783.
- 912 Singh, S.C., Crawford, W.C., Carton, H., Seher, T., Combier, V., Cannat, M., Canales, J.P.,  
913 Düsünür, D., Escartín, J., and Miranda, J., 2006, Discovery of a magma chamber and  
914 faults beneath a Mid-Atlantic Ridge hydrothermal field: *Nature*, v. 442, p. 1029–  
915 1032.
- 916 Smith, D.K., and Cann, J.R., 1990, Hundreds of small volcanoes on the median valley floor  
917 of the Mid-Atlantic Ridge: *Nature*, v. 344, p. 427–431.
- 918 Smith, D.K., Cann, J.R., and Escartín, J., 2006, Widespread active detachment faulting and  
919 core complex formation near 13°N on the Mid-Atlantic Ridge: *Nature*, v. 443, p.  
920 440–444, doi:10.1038/04950.
- 921 Thurnherr, A.M., Reverdin, G., Bouruet-Aubertot, P., St. Laurent, L.C., Vangriesheim, A.,  
922 and Ballu, V., 2008, Hydrography and flow in the Lucky Strike segment of the Mid-  
923 Atlantic Ridge: *Journal of Marine Research*, v. 66, p. 347–372.

- 924 Wilson, C., Charlou, J.-L., Ludford, E., Klinkhammer, G., Chin, C., Bougault, H., German, C.,  
925 Speer, K., and Palmer, M., 1996, Hydrothermal anomalies in the Lucky Strike  
926 segment on the Mid-Atlantic Ridge (37°17'N): Earth and Planetary Science Letters,  
927 v. 142, p. 467–477.
- 928 Yeo, I., Searle, R.C., Achenbach, K.L., Le Bas, T.P., and Murton, B.J., 2011, Eruptive  
929 hummocks: Building blocks of the upper ocean crust: *Geology*, v. 40, no. 1, p. 91–94,  
930 doi: 10.1130/G31892.1.
- 931